Size effects in wedge indentation predicted by a gradient-enhanced crystal-plasticity model*

M.J. Lewandowski and S. Stupkiewicz†

Institute of Fundamental Technological Research, Polish Academy of Sciences,

Pawińskiego 5b, 02-106 Warsaw, Poland

Abstract

A recently developed gradient-enhanced crystal-plasticity model is applied to predict the size effects in wedge indentation. In the model, the internal length scale is defined through standard quantities that appear in the underlying non-gradient hardening law. A careful calibration of the non-gradient hardening law is thus performed, and the model is validated against published experimental results. To this end, a comprehensive computational study of wedge indentation into a nickel single crystal is performed, and the obtained results show a good agreement with the experiment in terms of the load–penetration depth curves for three wedge angles, as well as in terms of the distributions of lattice rotation, GND density, and net Burgers vector. For the indentation depth of about 200 µm, as employed in the experiment, the predicted size effects are insignificant. Accordingly, the size effects are next studied for the indentation depth varied between 200 µm and 1 µm. As an intermediate result, apparently not published to date, the general 3D crystal plasticity model with anisotropic hardening is consistently reduced to a 2D plane-strain model in which plastic deformation is realized by three effective in-plane slip systems, each representing two crystallographic slip systems.

Keywords: Indentation size effect; Geometrically necessary dislocations; Crystal plasticity; Gradient plasticity; Finite-element method

1 Introduction

A considerable interest in the materials science and mechanics communities is currently focused on size effects in metal plasticity. Size effects induced by strain gradients are observed in micro-torsion (Fleck et al., 1994), micro-bending (Stölken and Evans, 1998) and micro/nano-indentation (Ma and Clarke, 1995; McElhaney et al., 1998; Pharr et al., 2010). It is commonly agreed that the related hardening mechanism ('smaller is stronger') is associated with the geometrically necessary dislocations (GNDs) that accommodate the strain gradients (Nye, 1953; Ashby, 1970). The strain gradients increase with decreasing sample size or indentation depth, and the additional GND hardening is then responsible for the related size effects. Size effects can also be observed in the absence of strain gradients, e.g., due to dislocation starvation in small samples (Greer and Nix, 2006). Those effects are, however, not considered in this work.

*Published in *Int. J. Plasticity*, vol. 109, pp. 54–78, 2018, doi: 10.1016/j.ijplas.2018.05.008

†Corresponding author, email: sstupkie@ippt.pan.pl

Instrumented indentation is a highly versatile and popular testing technique, and hence the indentation size effect is by far the most frequently studied size effect. For geometrically self-similar indenters, like pyramids and cones, the usual size effect manifests itself in the increase of hardness, defined as the ratio of the load to the projected contact area, with decreasing indentation depth (Pharr et al., 2010). The indentation size effect is also characteristic for spherical indentation (Swadener et al., 2002), where the hardness increases with decreasing indenter radius (for a fixed ratio of the indentation depth to the indenter radius).

Size-dependent response has also been observed in wedge indentation. Chen et al. (2012) performed indentation of an aluminum single crystal by a series of diamond wedges and reported a significant increase of hardness for the indentation depth below 1–2 µm, while the response was essentially size-independent for the indentation depth above 5 µm. Notably, the wedge indentation technique is definitely less popular than the usual Berkovich or spherical tip indentation. The work of Chen et al. (2012) is apparently the only one showing the size effects in wedge indentation experimentally.

In wedge indentation, an adequately oriented single crystal is deformed in (approximately) plane-strain conditions. This offers significant benefits for both experiment and modelling, as discussed below. A wedge indentation technique accompanied by a detailed characterization of lattice rotations using electron backscatter diffraction (EBSD) has been developed by Kysar et al. (2007, 2010). In this technique, the specimen midplane is exposed after indentation, and the in-plane rotations near the indent are measured with a high resolution. In the experiment, the indentation depth was close to 200 µm, which facilitated high-resolution EBSD measurements. However, as the indentation depth was relatively large, the overall response is not expected to be affected by size effects. Further processing of the measured rotation field delivers additional valuable data such as the spatial distributions of the total and slip-system-resolved GND densities (Kysar et al., 2010) and the magnitude and orientation of the net Burgers vector density (Sarac et al., 2016). The technique is quite unique to the wedge indentation because it relies on the plane-strain assumption. Note that full-field measurements of lattice rotations in the vicinity of three-dimensional indents are readily available (Zaafarani et al., 2006; Rester et al., 2008). However, more involved techniques are then needed to estimate the GND density, and the achievable resolution is lower (Demir et al., 2009; Wilkinson and Randman, 2010).

From the modelling point of view, with the focus on crystal plasticity, the wedge indentation is also quite advantageous because the problem can be formulated as a two-dimensional (2D) one thus offering a significant reduction of the computational cost compared to the three-dimensional (3D) setting in the usual Berkovich or spherical tip indentation. For a face-centred cubic (fcc) crystal deformed within the (1 1 0) plane, the crystal plasticity model itself can also be simplified by introducing three effective, composite in-plane slip systems, each representing two crystallographic slip systems (Rice, 1987). This feature has actually been exploited in the wedge indentation experiments of Kysar et al. (2007, 2010). The crystal and the wedge were adequately oriented such that the plane-strain deformation with three composite slip systems could be assumed in the processing of the EBSD measurements. The reduction of the number of slip systems in an fcc crystal from 12 to 3 becomes particularly advantageous when it comes to the modelling of size effects using a gradient crystal plasticity model. Indeed, in many formulations of gradient crystal plasticity (including the one used in this work), the slip rates on individual slip systems (or related variables, e.g., the dislocation densities on individual slip systems) constitute the global unknowns in a boundary value problem. For an fcc crystal, the 3D model involves thus 15 global unknowns (3 displacements and 12 slip rates), while the reduced 2D model involves 5 global unknowns (2 displacements and 3 slip rates). The saving in the computational cost associated with the

transition from 3D to 2D is thus substantial.

In the case of the classical (size-independent) crystal plasticity, full 3D simulation of indentation does not constitute a major problem at the current stage of development of computational methods. An overview of the related literature can be found in Petryk et al. (2017) along with a methodology for estimating the strain hardening exponent based on the analysis of the pile-up/sink-in pattern around the residual impression after spherical indentation.

However, modelling of the indentation size effect is in most cases limited to isotropic plasticity (e.g., Huang et al., 2000, 2006; Qu et al., 2006), often based on a simplified geometrical model (e.g., Nix and Gao, 1998; Abu Al-Rub, 2007). Simulations based on crystal plasticity with an internal length scale are much more scarce, even if a considerable number of gradient crystal-plasticity models are available in the literature, for instance, those of Gurtin (2000), Forest et al. (2002), Evers et al. (2004), Han et al. (2005), Kuroda and Tvergaard (2008), Bargmann et al. (2011), Hochrainer et al. (2014), Anand et al. (2015), Wulfinghoff et al. (2015), and Kratochvil and Kruzik (2016), to mention just a few representative examples. To the best of our knowledge, the only 3D gradient crystal-plasticity simulations of indentation are those of Lee and Chen (2010) and Gao et al. (2015), in each case employing a version of the so-called conventional mechanism-based strain gradient (crystal) plasticity theory (Huang et al., 2004; Han et al., 2005), and the recent simulations by Stupkiewicz and Petryk (2016), which employ the gradient-enhanced crystal-plasticity model developed by Petryk and Stupkiewicz (2016).

The model of Petryk and Stupkiewicz (2016) is also employed in the present work. In this model, the classical framework of crystal plasticity (Hill, 1966; Rice, 1971; Hill and Rice, 1972) is enhanced with slip-rate gradient effects by extending the usual anisotropic hardening law with a single isotropic term that represents the GND hardening. In contrast to the frequently used split of the total dislocation density into the densities of statistically stored dislocations (SSDs) and GNDs (e.g., Ashby, 1970; Fleck and Hutchinson, 1993; Nix and Gao, 1998), the model employs such a split applied in an incremental form only. This apparently minor difference has a significant influence on the resulting model. The internal length scale, which is derived in a closed form and depends on the current flow stress and hardening rate, is shown to be closely related to the mean free path of dislocations and thus possesses a direct physical interpretation. The resulting 'minimal' gradient enhancement of the hardening law is free of any fitting parameters. The computational treatment of the model relies on element-scale averaging of local slip rates, and the resulting non-local slip rates are used to compute the slip-rate gradients that govern the GND hardening. The averaging involves an independent length-scale parameter of purely numerical (or regularization) nature. Spherical indentation into a copper single crystal has been simulated, and the predicted dependence of hardness on the indenter radius shows a good agreement with experiment (cf., Stupkiewicz and Petryk, 2016).

In this paper, the gradient-enhanced crystal plasticity model of Petryk and Stupkiewicz (2016) is applied to predict the size effects in wedge indentation. Specifically, the effect of the indentation depth on the hardness, residual imprint and sink-in, lattice rotation and GND distribution is examined for the wedge indentation into a nickel single crystal. To the best of our knowledge, results of such scope have not been reported so far. Apparently, the only related simulations of wedge indentation are those of Reuber et al. (2014) and Bittencourt (2018). Reuber et al. (2014) used a nonlocal crystal plasticity model that includes dislocation transport. With reference to the experiment of Kysar et al. (2010), the simulation comprised only the indentation depth of 200 µm and only the 90° wedge, and a systematic study of size effects was not performed. A version of the strain-gradient crystal-plasticity model of Gurtin (2008) was employed in the simulations of Bittencourt (2018).

The wedge angle was varied between 140° and 170°, hence relatively shallow indentations were analyzed, and no direct reference was made to experiment, the analysis being focused on qualitative effects of the hardening model and lattice rotation. Let us mention that wedge indentation is a suitable problem that can be studied using the 2D discrete dislocation dynamics (DDD) method. The DDD models are inherently size-dependent. However, in view of the underlying small-strain assumption, the DDD simulations are restricted to shallow indentations with the wedge angle close to 180° (e.g., Balint et al., 2006; Kreuzer and Pippan, 2007; Zhang et al., 2014).

The present study of size effects is preceded by a detailed validation of the model against the experimental results reported by Dahlberg et al. (2014) and Sarac et al. (2016) for a nickel single crystal indented by three wedges of varying wedge angle. In the experiment, the indentation depth is about 200 µm so that the response is practically not influenced by size effects, and the validation actually concerns the underlying non-gradient model. As already discussed, the experimental results include not only the load–penetration depth curves, but also a full-field characterization of lattice rotations, GND density, and net Burgers vector. The full set of available experimental data is used for validation, and a good agreement of the model predictions with the experiment is demonstrated for the three wedge angles. Such a comprehensive study of the wedge indentation experiments has not been reported to date, even if selected features have already been successfully reproduced by (size-independent) crystal plasticity simulations (Kysar et al., 2010; Dahlberg et al., 2014; Sarac et al., 2016). Importantly, calibration of the hardening law has been here performed using independent data available in the materials science literature, and only one parameter, the initial critical resolved shear stress, has been adjusted such that the indentation load–penetration depth curve predicted for the 120° wedge matches the experimental one.

The present simulations are carried out using the plane-strain crystal-plasticity model that involves three composite in-plane slip systems. In Section 2.4 we show, apparently for the first time, how to consistently reduce the full 3D model of crystal plasticity with anisotropic hardening to the 2D plane-strain model for an fcc crystal deformed within the (1 1 0) plane. While the general structure of the model is not affected by the reduction, the effective slip-system interaction matrix takes a nontrivial form, and the effective slip rate turns out to be equal to a weighted sum of the slip rates on the individual composite in-plane slip systems.

The paper is organized as follows. The classical framework of crystal plasticity at finite strain is first recalled in Section 2, followed by a concise description of the 'minimal' gradient enhancement proposed recently by Petryk and Stupkiewicz (2016), Section 2.3. In Section 2.4, the 3D crystal plasticity model is consistently reduced to the 2D plane-strain model. The finite-element implementation of the model is discussed in Section 3. A comprehensive finite-element study of wedge indentation into a nickel single crystal is reported in Section 4. First, the hardening law is calibrated, and the model predictions are then compared to the experimental results of Dahlberg et al. (2014) and Sarac et al. (2016). In Section 5, simulations are carried out for the indentation depth ranging from 200 µm down to 1 µm, and the related size effects are examined, in particular, the dependence of hardness, residual imprint and lattice rotation on the indentation depth. In Appendices A and B, parametric studies are carried out to examine the influence of friction and of the regularization scheme in the crystal plasticity model. Finally, the secondary effect of the numerical length-scale parameter on the predicted size effects is illustrated in Appendix C.

2 Crystal plasticity model

2.1 Classical crystal plasticity framework

In the classical theory of crystal plasticity (Hill, 1966; Rice, 1971; Hill and Rice, 1972), the kinematics is based upon the multiplicative split of the deformation gradient $\mathbf{F}$ (Kröner, 1960; Lee, 1969),

$$\mathbf{F} = \mathbf{F}^* \mathbf{F}^p, \qquad \mathbf{F}^* = \mathbf{R}^* \mathbf{U}^e, \tag{1}$$

where $\mathbf{F}^p$ is the plastic part of the deformation gradient, and $\mathbf{F}^*$ is further decomposed into elastic stretch $\mathbf{U}^e$ and rotation $\mathbf{R}^*$. Further, plastic deformation is assumed to result from plastic slip on crystallographic slip systems,

$$\dot{\mathbf{F}}^p = \mathbf{L}^p \mathbf{F}^p, \qquad \mathbf{L}^p = \sum_{\alpha=1}^{N_s} \dot{\gamma}_\alpha \mathbf{s}_\alpha \otimes \mathbf{m}_\alpha, \tag{2}$$

where orthogonal unit vectors $\mathbf{s}_\alpha$ and $\mathbf{m}_\alpha$ define slip system α with $\mathbf{s}_\alpha$ being the slip direction and $\mathbf{m}_\alpha$ the slip plane normal. Here, we adopt the convention that plastic slip rate $\dot{\gamma}_\alpha$ can be positive or negative. The corresponding number of slip systems in a face-centred cubic (fcc) crystal is thus $N_s = 12$.

As the elastic strains are small in ductile crystals (except at very high hydrostatic pressure, which is not the case here), the elastic response is assumed to be governed by the simple anisotropic St. Venant–Kirchhoff model,

$$\mathbf{P}^e = \mathbb{L}\mathbf{E}^e, \qquad \mathbf{E}^e = \frac{1}{2}\left(\mathbf{C}^e - \mathbf{I}\right), \qquad \mathbf{C}^e = (\mathbf{U}^e)^2 = (\mathbf{F}^*)^{\mathrm{T}}\mathbf{F}^*, \tag{3}$$

where $\mathbb{L}$ is a fourth-order elastic stiffness tensor, and $\mathbf{P}^e$ is the symmetric second Piola–Kirchhoff stress tensor relative to the intermediate configuration, so that $\mathbf{P}^e$ is here linear in the elastic Green–Lagrange strain tensor $\mathbf{E}^e$. The second Piola–Kirchhoff stress $\mathbf{P}^e$ is related to the Cauchy stress $\boldsymbol{\sigma}$ and Mandel stress $\mathbf{M}$ as follows,

$$\boldsymbol{\sigma} = (\det \mathbf{F}^*)^{-1} \mathbf{F}^* \mathbf{P}^e (\mathbf{F}^*)^{\mathrm{T}}, \qquad \mathbf{M} = \mathbf{C}^e \mathbf{P}^e, \tag{4}$$

where the Mandel stress $\mathbf{M}$ is of particular importance because it is energetically conjugate to the plastic velocity gradient $\mathbf{L}^p$, Eq. (2).

The Schmid-type yield condition, accompanied by the flow rule and complementarity condition,

$$f_\alpha = |\tau_\alpha| - \tau_\alpha^c \leq 0, \qquad \operatorname{sign}(\tau_\alpha)\dot{\gamma}_\alpha \geq 0, \qquad \dot{\gamma}_\alpha f_\alpha = 0, \tag{5}$$

is defined individually for each slip system in terms of the resolved shear stress τ_α,

$$\tau_\alpha = \mathbf{M} \cdot (\mathbf{s}_\alpha \otimes \mathbf{m}_\alpha), \tag{6}$$

and the critical resolved shear stress τ_α^c, the evolution of which is described by the hardening law to be discussed later. Note that kinematic hardening can be included in the above framework by introducing a back-stress ξ_α into the yield condition, so that $f_\alpha = |\tau_\alpha - \xi_\alpha| - \tau_\alpha^c$, along with an evolution law for ξ_α. The back-stress effects are essential in the case of cyclic and non-proportional loading, while predominantly monotonic strain paths are encountered in the indentation problem considered in this work. Accordingly, the related effects are not considered here.

The rate-independent model described above suffers from the well-known problem of non-uniqueness in the selection of active slip systems. The problem can be overcome by applying the incremental energy minimization framework (e.g., Ortiz and Stainier, 1999; Petryk and Kursa, 2015), which, however, is not easily applicable in finite-element computations for general multislip crystal plasticity. Accordingly, regularized models are usually used in practice, and two such models (both are employed in this work) are summarized below.

2.1.1 Rate-dependent regularization of Schmid law

The classical approach, widely used in literature is based upon the viscous regularization proposed by Hutchinson (1976). In this regularization scheme, each slip rate $\dot{\gamma}_\alpha$ is assumed to be a (highly nonlinear) function of the corresponding resolved shear stress τ_α,

$$\dot{\gamma}_\alpha = \dot{\gamma}_0 \operatorname{sign}(\tau_\alpha) \left(\frac{|\tau_\alpha|}{\tau_\alpha^c} \right)^m . \tag{7}$$

Two additional material parameters are here introduced, namely the reference slip rate $\dot{\gamma}_0$, usually assumed constant for all slip systems, and exponent $m \gg 1$ that describes rate sensitivity. In this approach, there is no elastic domain, and all slip systems are simultaneously active.

In the alternative, Perzyna-like rate-dependent regularization of the Schmid law, the slip rate is a function of the overstress and vanishes when the stress stays inside the elastic domain (e.g., Asaro, 1983; Sabnis et al., 2013). That approach will not be pursued in this work.

2.1.2 Rate-independent regularization of Schmid law

Following Arminjon (1991) and Gambin (1992), a rate-independent regularization can be obtained by introducing a single yield condition for all slip systems,

$$F = \left(\sum_{\alpha=1}^{N_s} \left(\frac{\tau_\alpha}{\tau_\alpha^c} \right)^{2n} \right)^{\frac{1}{2n}} - 1 \leq 0, \tag{8}$$

where $n \gg 1$ is an integer, and it is the only additional parameter with respect to the original model. The non-smooth convex domain defined by the collection of yield conditions $f_\alpha \leq 0$ is thus replaced by a single smooth and convex domain inscribed in the original domain. Plastic flow is then governed by the associated flow rule of Mandel's type (Mandel, 1971),

$$\mathbf{L}^p = \dot{\zeta} \frac{\partial F}{\partial \mathbf{M}}, \qquad \dot{\zeta} \geq 0, \qquad \dot{\zeta} F = 0, \tag{9}$$

where $\dot{\zeta}$ is the plastic multiplier that satisfies the usual complementarity condition. It follows that the plastic velocity gradient $\mathbf{L}^p$ has exactly the form $(2)_2$ characteristic for crystal-plasticity models, namely

$$\mathbf{L}^p = \sum_{\alpha=1}^{N_s} \dot{\gamma}_\alpha \mathbf{s}_\alpha \otimes \mathbf{m}_\alpha, \qquad \dot{\gamma}_\alpha = \underbrace{\left(\sum_{\beta=1}^{N_s} \left(\frac{\tau_\beta}{\tau_\beta^c} \right)^{2n} \right)^{\frac{1}{2n}-1}}_{} \frac{\dot{\zeta}}{\tau_\alpha^c} \left(\frac{\tau_\alpha}{\tau_\alpha^c} \right)^{2n-1} . \tag{10}$$

Even though it is not apparent, the dependence of $\dot{\gamma}_\alpha$ on τ_α in Eq. $(10)_2$ is of exactly the same form as that in the rate-dependent model (7). The difference is that here the reference slip rate is not constant and it is different for each slip system. In particular, it depends on the plastic multiplier $\dot{\zeta}$ that is determined from the usual consistency condition $\dot{F} = 0$.

Note that the underbraced term in Eq. $(10)_2$ is equal to unity when $F = 0$, and it can be skipped in the rate formulation. However, when the solution of incremental equations is sought, this term is not equal to unity until the solution is found, and, according to our experience, skipping the underbraced term deteriorates the convergence behaviour of the iterative scheme (but does not affect the actual solution).

2.2 Hardening law

Evolution of the critical resolved shear stresses τ_α^c is described by the following hardening law,

$$\dot{\tau}_\alpha^c = \sum_{\beta=1}^{N_s} h_{\alpha\beta}|\dot{\gamma}_\beta| = \theta \sum_{\beta=1}^{N_s} q_{\alpha\beta}|\dot{\gamma}_\beta|, \tag{11}$$

where the hardening matrix $h_{\alpha\beta}$ can be specified directly, or it can be equivalently expressed in terms of the isotropic hardening modulus θ and dimensionless interaction matrix $q_{\alpha\beta}$, thus $h_{\alpha\beta} = \theta q_{\alpha\beta}$. The interaction matrix $q_{\alpha\beta}$ may be specified in numerous manners, for instance, taking into account coplanar, collinear or cross slip effects (Franciosi and Zaoui, 1982; Bassani and Wu, 1991). In this work, the interaction matrix is defined such that only self-hardening is distinguished from latent hardening on distinct slip systems. Accordingly, we have $q_{\alpha\beta} = 1$ for $\alpha = \beta$ and $q_{\alpha\beta} = q$ for $\alpha \neq \beta$, where q is a material parameter, so that the interaction matrix is equal to $q_{\alpha\beta} = q + (1-q)\delta_{\alpha\beta}$. Note that special care must be taken when the general 3D model is reduced to a 2D plane-strain model, see Section 2.4.

In the subsequent presentation of the gradient enhancement of the hardening law, it is convenient to define the hardening law by specifying the dependence of the hardening modulus θ on the flow stress τ defined such that

$$\dot{\tau} = \theta\dot{\gamma}, \qquad \dot{\gamma} = \sum_{\alpha=1}^{N_s} |\dot{\gamma}_\alpha|, \tag{12}$$

where $\dot{\gamma}$ is the effective slip rate, and τ is interpreted as the isotropic part of the critical resolved shear stresses τ_α^c, since the anisotropic hardening law (11) can be equivalently written as

$$\dot{\tau}_\alpha^c = \dot{\tau} + \theta \sum_{\beta=1}^{N_s} (q_{\alpha\beta} - 1)|\dot{\gamma}_\beta|. \tag{13}$$

The constitutive function that specifies the dependence of θ on τ is adopted here in the following bilinear form,

$$\theta = \theta_\tau(\tau) = \max(\theta_{III}(\tau), \theta_{IV}), \qquad \theta_{III}(\tau) = \theta_0 \left(1 - \frac{\tau}{\tau_{max}}\right), \qquad \tau \geq \tau_0 \geq 0, \tag{14}$$

where $\theta_{III}(\tau)$ corresponds to a linear decrease of θ with increasing τ, which is characteristic for stage III hardening, θ_{IV} is a constant hardening modulus, which is characteristic for stage IV hardening, and τ_0, τ_{max}, θ_0 and θ_{IV} are material parameters. The reasons behind considering only stage III and stage IV hardening are discussed in Section 4.1 along with the calibration of the hardening law (14) for nickel.

By integrating the evolution law $(12)_1$ with $\tau = \tau_0$ for $\gamma = 0$, the hardening law, known as the Voce law, is obtained in the following form,

$$\tau = \tau_\gamma(\gamma) = \tau_0 + (\tau_{max} - \tau_0)\left(1 - \exp\left(\frac{-\theta_0\gamma}{\tau_{max}}\right)\right), \qquad 0 \leq \gamma \leq \gamma_{IV}, \tag{15}$$

where γ_{IV} corresponds to the transition from stage III to stage IV hardening. For $\gamma > \gamma_{IV}$, the hardening modulus is constant, $\theta = \theta_{IV}$, and thus the flow stress τ increases linearly with increasing γ.

2.3 Gradient-enhanced hardening law

A gradient enhancement of the classical hardening law has been recently proposed by Petryk and Stupkiewicz (2016), see also Stupkiewicz and Petryk (2016) for the details of its computational treatment. This model is used in the present work, and it is briefly presented below. For the detailed derivation, the reader is referred to Petryk and Stupkiewicz (2016).

In the present 'minimal' gradient enhancement, the effect of slip-rate gradients and the related additional hardening due to GNDs are included only in the isotropic part of the hardening law, through the following enhancement of the hardening law $(12)_1$,

$$\dot{\tau} = \theta(\dot{\gamma} + \ell\dot{\chi}), \tag{16}$$

where $\dot{\chi}$ is the effective slip-rate gradient (to be specified below), and ℓ is the characteristic length that has been *derived* in the following explicit form,

$$\ell = \frac{a^2\mu^2 b}{2\tau\theta}. \tag{17}$$

The above gradient enhancement has been derived by exploiting the classical Taylor formula (Taylor, 1934),

$$\tau = a\mu b\sqrt{\rho}, \tag{18}$$

which relates the flow stress τ to the dislocation density ρ, where the strengthening parameter a, the shear modulus μ, and the Burgers vector modulus b are known parameters. The second fundamental concept leading to the gradient enhancement (16)–(17) is the split of the total dislocation density into the contributions of SSDs and GNDs, here applied in the *rate* form, in distinction to the usual split of the total density itself (e.g., Ashby, 1970; Fleck and Hutchinson, 1993; Nix and Gao, 1998). As discussed in detail by Petryk and Stupkiewicz (2016), the characteristic length ℓ possesses a direct physical interpretation and is closely linked to the mean free path of dislocations. Furthermore, it is explicitly expressed through the current flow stress τ and hardening modulus θ (thus ℓ evolves during deformation), and through known parameters a, μ and b, so that, once the hardening law $\theta = \theta_\tau(\tau)$ is specified, no further assumption nor extra parameter is needed to define the characteristic length ℓ.

The gradient-enhanced anisotropic hardening law is finally obtained by combining the gradient-enhanced isotropic hardening law (16) with the non-gradient anisotropic hardening law (13), viz.

$$\dot{\tau}^c_\alpha = \theta\left(\sum_{\beta=1}^{N_s} q_{\alpha\beta}\big|\dot{\gamma}_\beta\big| + \ell\dot{\chi}\right). \tag{19}$$

The gradient effects enter the enhanced hardening law (19) through the effective slip-rate gradient $\dot{\chi}$ which has been postulated by Petryk and Stupkiewicz (2016) in the following form,

$$\dot{\chi} = \|\overset{\diamond}{\mathbf{G}}\|, \qquad \overset{\diamond}{\mathbf{G}} = \sum_{\alpha=1}^{N_s} \mathbf{s}_\alpha \otimes (\nabla^{\#}\dot{\gamma}_\alpha \times \mathbf{m}_\alpha), \qquad \nabla^{\#}\dot{\gamma}_\alpha = (\mathbf{F}^p)^{-\mathrm{T}}\,\nabla\dot{\gamma}_\alpha, \tag{20}$$

where $\mathbf{G}$ is the dislocation density tensor (Cermelli and Gurtin, 2001), and $\overset{\diamond}{\mathbf{G}}$ is its plastically convected (Oldroyd) derivative,

$$\overset{\diamond}{\mathbf{G}} = \dot{\mathbf{G}} - \mathbf{L}^p\mathbf{G} - \mathbf{G}(\mathbf{L}^p)^{\mathrm{T}}. \tag{21}$$

In Eq. (20), $\nabla\dot{\gamma}_\alpha$ denotes the reference gradient of slip rate $\dot{\gamma}_\alpha$ and $\nabla^{\#}\dot{\gamma}_\alpha$ its push-forward to the intermediate local configuration. The dislocation density tensor $\mathbf{G}$ characterizes incompatibility of $\mathbf{F}^p$ and is the finite-strain counterpart of the classical Nye's tensor $\boldsymbol{\alpha}$ (Nye, 1953; Kröner, 1962). In the small-strain framework, the evolution law (20) for $\dot{\chi}$ would thus reduce to $\dot{\chi} = \|\dot{\boldsymbol{\alpha}}\|$, where $\dot{\boldsymbol{\alpha}} = \sum_\alpha \mathbf{s}_\alpha \otimes (\nabla\dot{\gamma}_\alpha \times \mathbf{m}_\alpha)$, see Petryk and Stupkiewicz (2016) for the details. Note that, as desired, the effective slip-rate gradient $\dot{\chi}$ defined above is not affected by the slip-rate gradients normal to the respective slip planes and only depends on the in-plane gradients that are accommodated by GNDs (Ashby, 1970).

Concluding, the simple gradient enhancement of the classical crystal plasticity amounts to replacing the hardening law (11) by its gradient-enhanced form (19) in which slip-rate gradients are included through the effective slip-rate gradient $\dot{\chi}$, Eq. (20). At the same time, the model is formulated in the framework of classical continua so that it does not involve any additional balance equations. The characteristic length ℓ has been derived in closed form (17), and this natural length scale evolves during the deformation process. This is a distinctive feature of the present model[1] as compared to many existing models in which the characteristic length is an independent (and constant) model parameter. Otherwise, the gradient enhancement is extremely simple—it has been termed 'minimal' by Petryk and Stupkiewicz (2016)—and, obviously, the model does not include various effects that have already been included in more elaborate models. In particular, the gradient-dependent back-stress effect (e.g. Gurtin, 2000; Evers et al., 2004) is not included so that the model is more suited for predominantly monotonic deformation processes, such as the indentation problem studied here.

As discussed by Stupkiewicz and Petryk (2016), the uniqueness of the incremental solution to a boundary-value problem is not ensured for the gradient-enhanced model in the form presented above. In particular, spatial jumps in slip-rate gradients are not excluded, which may lead to oscillatory solutions, as illustrated by the analytical solution to a one-dimensional boundary-layer problem, cf. Stupkiewicz and Petryk (2016). A kind of regularization is thus needed, and a suitable regularization approach is described in Section 3.

2.4 Consistent reduction to a 2D plane-strain model

As shown by Rice (1987), plane-strain conditions can be adopted as an approximation of elastic-plastic deformation of an fcc single crystal loaded within the (1 1 0) plane, provided specimen geometry and loading admit those plane-strain conditions. Plastic deformation is then realized by three effective, composite in-plane slip systems, each representing two crystallographic slip systems that are either coplanar or collinear. The two crystallographic slip systems in each pair experience the same resolved shear stress and are thus assumed to slip simultaneously and by the same amount, provided they have the same initial critical resolved shear stress. It is assumed that the remaining six crystallographic slip systems do not significantly contribute to the overall deformation and are thus assumed to be inactive.

In fact, the wedge indentation test (Kysar et al., 2007, 2010), see Fig. 1, has been deliberately designed to realize the above plane-strain conditions in a single-crystal specimen indented into the (0 0 1) plane by a wedge parallel to the [1 1 0] direction. EBSD measurements of lattice rotations in the specimen mid-plane have shown that the out-of-plane rotation is almost zero (Kysar et al., 2010; Sarac et al., 2016) thus confirming the validity of the assumption of plane-strain deformation.

In this section, the 3D crystal plasticity model described in the preceding subsections is consistently reduced to a 2D plane-strain model. The geometry of the composite in-plane slip systems has been detailed by Rice (1987), see also Kysar et al. (2010), and these considerations are also followed here. However, Rice (1987) considered an ideally plastic crystal and derived the corresponding (constant) yield locus. Here, we derive, apparently for the first time, the hardening law relating the effective in-plane quantities that is consistent with the original hardening law relating the crystallographic quantities. Here and in the following, we will use the name 'composite' in-plane slip rate (and 'composite' in-plane slip system) rather than the 'effective' one to avoid confusion with the effective slip rate $\dot{\gamma}$ and with the effective slip-rate gradient $\dot{\chi}$.

[1] See also Remark 2 in Petryk and Stupkiewicz (2016) for a comment on the difference with respect to the model of Nix and Gao (1998).

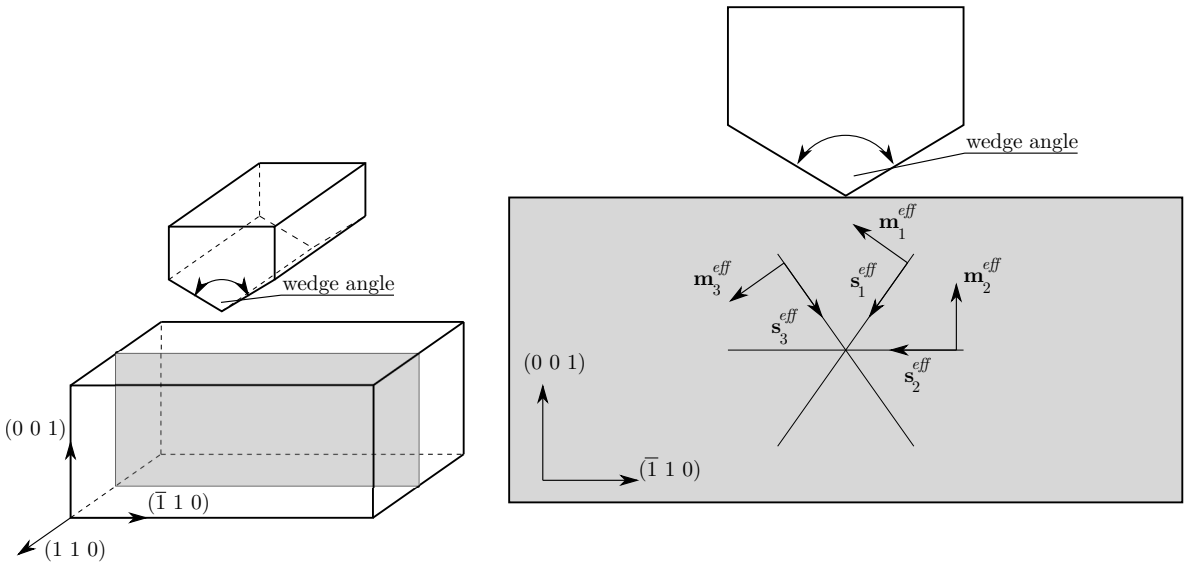

Figure 1: Scheme of the wedge indentation test. An fcc single crystal is deformed within the $(1\,1\,0)$ plane, and deformation is realized by three effective, composite in-plane slip systems.

As discussed above, only six crystallographic slip systems are potentially active in plane-strain conditions, and these are provided in Table 1. It is assumed here that the crystal deforms in the $(1\,1\,0)$ plane. In the following, the quantities related to the six crystallographic slip systems will be indexed by a Greek subscript, $\alpha, \beta = 1, \ldots, 6$, and the quantities related to the three composite in-plane slip systems will be indexed by an uppercase subscript, $A, B = 1, 2, 3$. Crystallographic slip systems 1 and 2 are coplanar, and the corresponding composite in-plane slip system ($A = 1$) shares the same $(1\,\bar{1}\,1)$ slip plane, while the composite in-plane slip direction is $[1\,\bar{1}\,\bar{2}]$. Crystallographic slip systems 5 and 6 are also coplanar, and the corresponding composite in-plane slip system ($A = 3$) shares the same $(1\,\bar{1}\,\bar{1})$ slip plane. Finally, crystallographic slip systems 3 and 4 are collinear, and the corresponding composite in-plane slip system ($A = 2$) shares the same $[1\,\bar{1}\,0]$ slip direction, while the composite slip plane is $(0\,0\,1)$. Slip planes and slip directions of the composite in-plane slip systems are provided in Table 2 along with the corresponding pairs (α, β) of crystallographic slip systems.

Table 1: Slip systems of an fcc crystal that are potentially active in plane-strain deformation in the $(1\,1\,0)$ plane.

α	1	2	3	4	5	6
$\mathbf{m}_\alpha$	$(1\,\bar{1}\,1)$	$(1\,\bar{1}\,1)$	$(1\,1\,1)$	$(\bar{1}\,\bar{1}\,1)$	$(1\,\bar{1}\,\bar{1})$	$(1\,\bar{1}\,\bar{1})$
$\mathbf{s}_\alpha$	$[1\,0\,\bar{1}]$	$[0\,\bar{1}\,\bar{1}]$	$[1\,\bar{1}\,0]$	$[1\,\bar{1}\,0]$	$[\bar{1}\,0\,\bar{1}]$	$[0\,1\,\bar{1}]$

Table 2: Composite in-plane slip systems in the $(1\,1\,0)$ plane.

A	1	2	3
$\mathbf{m}_A^{\mathit{eff}}$	$(1\,\bar{1}\,1)$	$(0\,0\,1)$	$(1\,\bar{1}\,\bar{1})$
$\mathbf{s}_A^{\mathit{eff}}$	$[1\,\bar{1}\,\bar{2}]$	$[1\,\bar{1}\,0]$	$[\bar{1}\,1\,\bar{2}]$
(α, β)	(1,2)	(3,4)	(5,6)

The effective resolved shear stress $\tau_A^{\mathit{eff}} = \mathbf{M} \cdot (\mathbf{s}_A^{\mathit{eff}} \otimes \mathbf{m}_A^{\mathit{eff}})$ on the composite in-plane slip system A is defined analogously to the one on the crystallographic slip system, cf. Eq. (6). The relationship between the effective

and crystallographic resolved shear stresses results from the geometry of slip systems, see Rice (1987), and can be written in the following form,

$$\tau_A^{eff} = \sum_{\alpha=1}^{6} \Lambda_{A\alpha} \tau_\alpha, \qquad \tau_A^{c,eff} = \sum_{\alpha=1}^{6} \Lambda_{A\alpha} \tau_\alpha^c, \tag{22}$$

which holds also for the critical resolved shear stresses, as expressed by Eq. $(22)_2$, and $\Lambda_{A\alpha}$ is here the transformation matrix,

$$\left[\Lambda_{A\alpha}\right] = \begin{bmatrix} \frac{1}{\sqrt{3}} & \frac{1}{\sqrt{3}} & 0 & 0 & 0 & 0 \\ 0 & 0 & \frac{\sqrt{3}}{2} & \frac{\sqrt{3}}{2} & 0 & 0 \\ 0 & 0 & 0 & 0 & \frac{1}{\sqrt{3}} & \frac{1}{\sqrt{3}} \end{bmatrix}. \tag{23}$$

It can be checked that the same (transposed) transformation matrix relates the crystallographic slip rates $\dot{\gamma}_\alpha$ and the composite in-plane slip rates $\dot{\gamma}_A^{eff}$, viz.

$$\dot{\gamma}_\alpha = \sum_{A=1}^{3} \Lambda_{A\alpha} \dot{\gamma}_A^{eff}, \tag{24}$$

and the effective slip rate $\dot{\gamma}$ is thus obtained in the following form,

$$\dot{\gamma} = \sum_{\alpha=1}^{6} |\dot{\gamma}_\alpha| = \sum_{\alpha=1}^{6} \sum_{A=1}^{3} \Lambda_{A\alpha} |\dot{\gamma}_A^{eff}| = \sum_{A=1}^{3} \lambda_A |\dot{\gamma}_A^{eff}|, \tag{25}$$

where vector λ_A is defined as follows,

$$\lambda_A = \sum_{\alpha=1}^{6} \Lambda_{A\alpha}, \qquad \left[\lambda_A\right] = \begin{bmatrix} \frac{2}{\sqrt{3}} & \sqrt{3} & \frac{2}{\sqrt{3}} \end{bmatrix}^T. \tag{26}$$

It follows that the effective slip rate $\dot{\gamma}$ is not a direct sum of the individual composite in-plane slip rates $\dot{\gamma}_A^{eff}$, but it involves the weights λ_A. This ensures that the hardening rate is consistently determined in the 2D model.

By combining Eqs. $(22)_2$, (11) and (24), we arrive at the hardening law that specifies the evolution of the effective critical resolved shear stresses $\dot{\tau}_A^{c,eff}$ in terms of the composite in-plane slip rates $\dot{\gamma}_A^{eff}$,

$$\dot{\tau}_A^{c,eff} = \theta \sum_{\alpha=1}^{6} \Lambda_{A\alpha} \sum_{\beta=1}^{6} q_{\alpha\beta} |\dot{\gamma}_\beta| = \theta \sum_{\alpha=1}^{6} \sum_{\beta=1}^{6} \Lambda_{A\alpha} q_{\alpha\beta} \sum_{B=1}^{3} \Lambda_{B\beta} |\dot{\gamma}_B^{eff}| = \theta \sum_{B=1}^{3} q_{AB}^{eff} |\dot{\gamma}_B^{eff}|, \tag{27}$$

where q_{AB}^{eff} is the effective interaction matrix,

$$q_{AB}^{eff} = \sum_{\alpha=1}^{6} \sum_{\beta=1}^{6} \Lambda_{A\alpha} q_{\alpha\beta} \Lambda_{B\beta}. \tag{28}$$

If the interaction matrix $q_{\alpha\beta}$ is defined as $q_{\alpha\beta} = q + (1-q)\delta_{\alpha\beta}$, cf. Section 2.2, then the effective interaction matrix q_{AB}^{eff} takes the following explicit form,

$$\left[q_{AB}^{eff}\right] = \begin{bmatrix} \frac{2}{3}(1+q) & 2q & \frac{4}{3}q \\ 2q & \frac{3}{2}(1+q) & 2q \\ \frac{4}{3}q & 2q & \frac{2}{3}(1+q) \end{bmatrix}. \tag{29}$$

Matrix q_{AB}^{eff} depends on the latent hardening parameter q in a nontrivial manner, which results from the geometry of the crystallographic and composite in-plane slip systems. Note that the effective self-hardening coefficients (i.e. those on the diagonal) are not equal to unity, and we have $q_{11}^{eff} = q_{33}^{eff} \neq q_{22}^{eff}$. Also, the off-diagonal interaction coefficients depend on the pair of composite in-plane slip systems considered.

Finally, the gradient-enhanced hardening law that governs the evolution of the effective resolved shear stresses $\dot{\tau}_A^{c,eff}$ takes the following form,

$$\dot{\tau}_A^{c,eff} = \theta\left(\sum_{B=1}^{3} q_{AB}^{eff}|\dot{\gamma}_B^{eff}| + \lambda_A \ell\dot{\chi}\right), \tag{30}$$

where the factor λ_A, Eq. (26), which scales here the gradient term $\ell\dot{\chi}$, results from the transformation rule $(22)_2$. It can be checked that the effective slip-rate gradient $\dot{\chi}$, Eq. (20), is expressed directly in terms of the respective composite in-plane quantities, namely

$$\dot{\chi} = \|\overset{\diamond}{\mathbf{G}}\|, \qquad \overset{\diamond}{\mathbf{G}} = \sum_{A=1}^{3} \mathbf{s}_A^{eff} \otimes (\nabla^{\#}\dot{\bar{\gamma}}_A^{eff} \times \mathbf{m}_A^{eff}). \tag{31}$$

With the above modifications, we arrive at the 2D plane-strain crystal-plasticity model that is fully consistent with the original 3D model. As shown above, the general structure of the reduced 2D model is identical to that of the original 3D model with the crystallographic slip systems simply replaced by the composite in-plane slip systems, see Table 3. However, the effective slip rate $\dot{\gamma}$, Eq. (25), the effective interaction matrix q_{AB}^{eff}, Eq. (28), and the gradient-enhancement term in the anisotropic hardening law, Eq. (30), must be adequately redefined in order to achieve the same hardening response.

Table 3: Governing equations of the reduced 2D model and the respective equations of the original 3D model.

	Original 3D model	Reduced 2D model
	Classical crystal-plasticity model	
Resolved shear stress	$\tau_\alpha = \mathbf{M}\cdot(\mathbf{s}_\alpha \otimes \mathbf{m}_\alpha)$	$\tau_A^{eff} = \mathbf{M}\cdot(\mathbf{s}_\alpha^{eff} \otimes \mathbf{m}_\alpha^{eff})$
Yield condition	$\lvert\tau_\alpha\rvert - \tau_\alpha^c \le 0$	$\lvert\tau_A^{eff}\rvert - \tau_A^{c,eff} \le 0$
Plastic flow rule	$\mathbf{L}^p = \sum_\alpha \dot{\gamma}_\alpha \mathbf{s}_\alpha \otimes \mathbf{m}_\alpha$	$\mathbf{L}^p = \sum_A \dot{\gamma}_A^{eff} \mathbf{s}_\alpha^{eff} \otimes \mathbf{m}_\alpha^{eff}$
Anisotropic hardening law	$\dot{\tau}_\alpha^c = \theta \sum_\beta q_{\alpha\beta}\lvert\dot{\gamma}_\beta\rvert$	$\dot{\tau}_A^{c,eff} = \theta \sum_B q_{AB}^{eff}\lvert\dot{\gamma}_B^{eff}\rvert$
Effective slip rate	$\dot{\gamma} = \sum_\alpha \lvert\dot{\gamma}_\alpha\rvert$	$\dot{\gamma} = \sum_A \lambda_A \lvert\dot{\gamma}_A^{eff}\rvert$
	Gradient enhancement	
Effective slip-rate gradient	$\dot{\chi} = \big\lVert\sum_\alpha \mathbf{s}_\alpha \otimes (\nabla^{\#}\dot{\gamma}_\alpha \times \mathbf{m}_\alpha)\big\rVert$	$\dot{\chi} = \big\lVert\sum_A \mathbf{s}_A^{eff} \otimes (\nabla^{\#}\dot{\gamma}_A^{eff} \times \mathbf{m}_A^{eff})\big\rVert$
Anisotropic hardening law	$\dot{\tau}_\alpha^c = \theta\big(\sum_\beta q_{\alpha\beta}\lvert\dot{\gamma}_\beta\rvert + \ell\dot{\chi}\big)$	$\dot{\tau}_A^{c,eff} = \theta\big(\sum_B q_{AB}^{eff}\lvert\dot{\gamma}_B^{eff}\rvert + \lambda_A\ell\dot{\chi}\big)$

3 Finite-element implementation

Below we briefly comment on the finite-element implementation of the gradient-enhanced crystal-plasticity model described in Section 2. The reduced 2D plane-strain model has been used in the actual simulations of wedge indentation, and we recall that its structure is the same as the structure of the full 3D model. The approach developed by Stupkiewicz and Petryk (2016) for the full 3D model is thus fully applicable and has been adopted here. Implementation of the non-gradient crystal-plasticity model, which has also been employed in the simulations, is standard and does not require separate description.

The model is formulated in the framework of classical continua, and the gradient enhancement is introduced only through the hardening law (19). The effective slip-rate gradient $\dot{\chi}$, which enters the hardening law, depends

on the slip-rate gradients $\nabla\dot{\gamma}_\alpha$, cf. Eq. (20), and the need to compute these gradients is the main difference with respect to the usual implementation of a non-gradient crystal-plasticity model. In the standard finite-element framework, the slip rates $\dot{\gamma}_\alpha$, or actually the increments $\Delta\gamma_\alpha$, are determined locally at the integration (Gauss) points, through the solution of the incremental constitutive equations, and their gradients are thus not available.

In the approach adopted here after Stupkiewicz and Petryk (2016), each local slip rate $\dot{\gamma}_\alpha$ is approximated by the respective continuous non-local slip rate $\dot{\bar{\gamma}}_\alpha$ that is governed by the following Helmholtz-type equation,

$$\dot{\bar{\gamma}}_\alpha - l_h^2 \nabla^2 \dot{\bar{\gamma}}_\alpha = \dot{\gamma}_\alpha, \tag{32}$$

where ∇^2 is the Laplace operator, and l_h is a length-scale parameter to be discussed below. The non-local slip rates $\dot{\bar{\gamma}}_\alpha$ are thus obtained by averaging the local slip rates $\dot{\gamma}_\alpha$ with l_h specifying the characteristic length in the averaging operation delivered by Eq. (32), cf. Peerlings et al. (1996). In the present finite-element implementation, the non-local slip rates $\dot{\bar{\gamma}}_\alpha$ constitute independent global unknowns that admit standard C^0-continuous interpolation. Evaluation of their gradients is thus immediate, and these gradients are used to compute the effective slip-rate gradient $\dot{\chi}$.

The numerical length-scale parameter l_h in Eq. (32) is here assumed to be proportional to the element size h, and it is thus independent of the physical length scale ℓ in the gradient-enhanced model. Specifically, by setting $l_h = h$, Eq. (32) provides element-scale averaging and smoothing of the local slip rates $\dot{\gamma}_\alpha$ that are defined at the element Gauss points only. Note that the popular implicit-gradient models of damage or softening plasticity (e.g., Peerlings et al., 1996) employ a Helmholtz-type equation identical to that in Eq. (32) with the aim to regularize the related strain-localization phenomena. However, in the implicit-gradient models, the length-scale parameter is assumed to be a material parameter as it specifies the thickness of the localization zone.

The length-scale parameter l_h can also be interpreted as a regularization parameter. In fact, the averaging equation (32) provides regularization which is needed in the model, as mentioned in Section 2.3 and as discussed in more detail in Stupkiewicz and Petryk (2016). Accordingly, instead of fixing the ratio of l_h to h, parameter l_h can be assumed to be a constant, like an additional model parameter. The influence of the regularization parameter l_h on the size effects predicted by the model is illustrated in Appendix C.

Equation (32) is accompanied by the standard homogeneous Dirichlet or Neumann boundary conditions, the latter being employed in the simulations reported below. It has been checked that the overall response in the wedge indentation problem studied in this work is not visibly affected by the boundary-condition type. This is because the boundary conditions influence the non-local slip rates $\dot{\bar{\gamma}}_\alpha$ only in the vicinity of the boundary, with the thickness of the corresponding boundary layer proportional to $l_h = h$. For a relatively fine mesh, as used in the present computations, the effect is negligible. Note that, in the case of the problem of a constrained half-space or layer subjected to shear, the homogeneous Dirichlet ('micro-clamped') boundary conditions prove effective in reproducing the boundary layers predicted by the analytical solution for the original model that does not employ the averaging equation (32), cf. Stupkiewicz and Petryk (2016).

The incremental constitutive equations are obtained by applying the implicit backward-Euler integration scheme. In the incremental setting, upon introducing the non-local slip increments $\Delta\bar{\gamma}_\alpha$ as independent global unknowns, the corresponding gradients $\nabla(\Delta\bar{\gamma}_\alpha)$, along with the current deformation gradient $\mathbf{F}$, are supplied to the local constitutive update procedure. The incremental constitutive equations are then solved with respect to the local unknowns which include the local slip increments $\Delta\gamma_\alpha$. The complete set of incremental constitutive equations can be found in Stupkiewicz and Petryk (2016).

Coupling of the non-local slip increments with the local ones is through Eq. (32) (in its incremental form), which is solved, for each slip system, at the global level together with the equilibrium equation. The global unknowns comprise thus the nodal displacements and the non-local slip increments (for an fcc crystal, 3+12 = 15 unknowns in 3D and 2 + 3 = 5 unknowns in a 2D plane-strain problem). The Newton method is used both at the global and local level thus leading to the classical nested iterative-subiterative scheme (Korelc and Wriggers, 2016).

In order to reduce the number of global degrees of freedom, a mixed order of interpolation has been adopted in the present implementation of the reduced 2D plane-strain model. The displacements are interpolated using the standard biquadratic shape functions (9-node quadrilaterals), and the non-local slip increments are interpolated using the bilinear shape functions. The element involves thus 18 displacement degrees of freedom and 12 degrees of freedom that represent the non-local slip increments. Mixed interpolation order is, in fact, a natural choice considering that slip increments are strain-like quantities, and the order of interpolation of strains (displacement gradients) is lower than that of displacements. This also leads to a significant reduction of the number of global unknowns, as compared to the case of equal interpolation order. The reduction would be even more pronounced in the 3D model in which 12 additional global unknowns are needed to represent the non-local slip increments. Note that, as the simplest approach, a low-order (trilinear) interpolation has been used by Stupkiewicz and Petryk (2016) for both displacements and non-local slip increments, in the former case combined with the F-bar enhancement.

Quadratic elements are known for a reasonably good performance in finite-strain nearly incompressible elasto-plasticity (e.g., Korelc et al., 2010). Thus there is no need for additional treatment (such as the enhanced-strain or F-bar formulation, reduced integration, etc.), which is necessary in the case of bilinear elements. Some tests involving quadratic elements from the serendipity family have been performed, but the fully-integrated biquadratic elements proved to perform better in the boundary value problems of the type considered here.

The model has been implemented using the *AceGen/AceFEM* package (Korelc, 2002; Korelc and Wriggers, 2016). *AceGen* is a code generation tool which takes advantage of the symbolic capabilities of *Mathematica* (www.wolfram.com) which are enhanced with the automatic differentation (AD) and expression optimization techniques. The AD technique implemented in *AceGen* has been employed to consistently linearize the nonlinear equations at the local (constitutive) and global (finite-element) level, which is crucial for achieving a good convergence behaviour of the nested iterative-subiterative Newton scheme. The computations have been carried out using *AceFEM*, a flexible finite-element code interfaced with *AceGen*.

Finally, we provide some details of the finite-element treatment of frictional contact interactions, which is a crucial ingredient of the wedge indentation problem studied in Section 4. The wedge indenter is modelled here as a rigid surface. This assumption is justifiable considering that the elastic deflections of the tungsten carbide wedge, as used in the experiment, are small compared to the finite elasto-plastic deformations of the nickel crystal beneath the indenter. To avoid excessively large strains and mesh distortion at the wedge tip, a rounded tip is actually used in the computations, as described in Section 4.

Preliminary tests have shown that the nodal enforcement of contact constraints leads, for the quadratic elements described above, to severe convergence problems. According to our experience, the crystal plasticity model is sensitive to sudden changes of boundary conditions, for instance, when a node comes into contact, and this caused the convergence problems mentioned above.

A significantly more robust scheme has been obtained by enforcing the contact constraints weakly in a manner

motivated by the mortar approach with dual quadratic Lagrange multipliers (Popp et al., 2012). Specifically, the unilateral contact conditions are enforced not on the normal gap evaluated at each node, but on the weighted gap defined as the integrated product of the gap and the dual Lagrange-multiplier basis function. Details of the formulation and the explicit formulae for the dual basis functions for quadratic elements can be found in Popp et al. (2012). Friction and tangential slip are treated accordingly, and the contact conditions are then enforced using the augmented Lagrangian technique (Alart and Curnier, 1991). The adopted approach results in a less stiff behaviour of contact elements, which proved crucial for successful simulations of the single-crystal wedge indentation problem studied in Section 4.

4 Simulation of wedge indentation into nickel single crystal

In this section, the crystal-plasticity model with and without the gradient enhancement in the hardening law is applied to simulate wedge indentation into a nickel single crystal, and the model predictions are compared to the recent experimental results reported by Dahlberg et al. (2014) and Sarac et al. (2016). Results of both models are reported even if their predictions do not differ significantly for the indentation depth of approximately 200 µm, as employed in the experiments (a separate study of size effects is reported in Section 5).

Calibration of the hardening law is described in Section 4.1. A detailed finite-element study of wedge indentation is then presented in Section 4.2. Supplementary results illustrating the effect of friction at the contact interface and the impact of regularization of the Schmid law are reported in Appendices A and B, respectively.

4.1 Calibration of the hardening law

The internal length scale ℓ introduced in the gradient-enhanced model of Section 2.3 depends on the current flow stress τ and hardening modulus θ, cf. Eq. (17), the other parameters (a, μ, b) being essentially known for a given material. It follows that the hardening law $\theta = \theta_\tau(\tau)$ governs, through ℓ, the size effects, and a physically-sound calibration of the hardening law is thus crucial for reliable predictions of the size effects. Our aim here is thus to calibrate the hardening law for pure nickel as much as possible in agreement with the data available in the materials science literature (Kocks, 1987; Haasen, 1958), while the experimental results from wedge indentation, both the load–depth curve and the lattice rotation data, will be used merely for validation of the calibrated hardening law.

The Voce-like hardening law (14) used in this work involves four parameters. Parameters $\theta_0 = 240\,\text{MPa}$ and $\tau_{max} = 150\,\text{MPa}$ have been determined using the experimental curve, taken from Kocks (1987, Fig. 13b), that represents the dependence of the hardening rate θ on the flow stress τ obtained for polycrystalline nickel. Specifically, the linear part of the experimental curve in the intermediate range of τ and θ, which corresponds to stage III hardening, has been approximated by the straight line that represents the Voce law (14), as shown in Fig. 2a.

This approach is commonly used, see Kocks and Mecking (2003); Sauzay and Kubin (2011), with the physical justification outlined below. The Voce hardening law describes well the relation between θ and τ during stage III. Focusing mostly on stage III hardening is justified since in multiple slip conditions stage I does not occur (Kocks and Mecking, 2003) and stage II hardening is less pronounced at room temperatures and

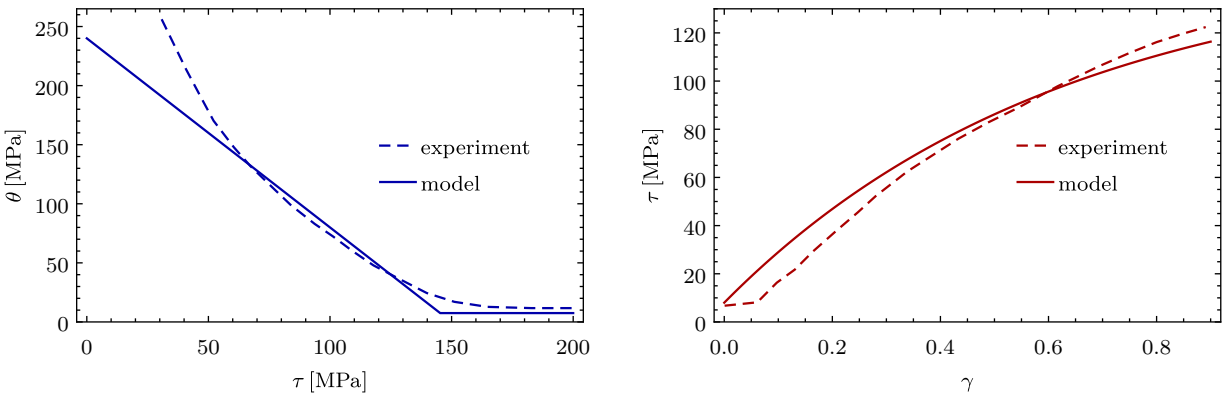

Figure 2: Calibration of the Voce hardening law: (a) calibration of parameters θ_0 and τ_{max} using the experimental data taken from Kocks (1987); (b) the calibrated hardening curve (corresponding to $\tau_0 = 8\,\mathrm{MPa}$) compared to the experimental one (Haasen, 1958).

with decreasing impurity content (Hollang, 2002). The value of $\theta_0 = 240\,\mathrm{MPa}$ obtained from our calibration falls well within the range of 1–2 $\times\, \mu/300$ (Sauzay and Kubin, 2011), where $\mu = (c_{11} - c_{12} + c_{44})/3 = 74.6\,\mathrm{GPa}$ is the shear modulus for the $\{1\,1\,1\}\langle 1\,\bar{1}\,0\rangle$-type slip systems. Also, the typical values of the constant stage II hardening rate θ_{II}, which is equal to the parameter θ_0 in the Voce hardening law (14), range from 195 MPa to 240 MPa (Haasen, 1958).

The constant stage IV hardening rate θ_{IV} has been adopted as the fraction of 0.05 of the parameter τ_{max}, thus $\theta_{IV} = 0.05\,\tau_{max} = 7.5\,\mathrm{MPa}$. Experimental observations show that the corresponding fraction is between 0.05 and 0.1 for many materials for different deformation modes (Kocks and Mecking, 2003), and the lower of the two values has been adopted here. Compared to the hardening law used by Stupkiewicz and Petryk (2016), where only stage III was considered for simplicity, the hardening law (14), which also includes stage IV, leads to a more robust computational model, according to our experience.

The remaining parameter of the Voce hardening law, i.e. the initial critical resolved shear stress τ_0, has been adjusted such that the experimental indentation load–penetration depth curve for the 120° wedge is correctly represented by the finite-element model described in the next subsection. Specifically, the value of $\tau_0 = 8\,\mathrm{MPa}$ proved to approximate the maximum indentation force well, as illustrated in Section 4.2, see Fig. 6c, and this value has been used in the computations. The 120° wedge has been used here for calibration because the influence of the wedge tip radius on the results is then the smallest.

Figure 2b shows the calibrated hardening curve (the flow stress τ as a function of the effective slip γ, cf. Eq. (15)) which shows a reasonable agreement with the experimental curve obtained at the room temperature (Haasen, 1958, Fig. 4). The experimental curve exhibits stage I of easy glide up to about 0.1 plastic shear, which is not reproduced by the Voce hardening law (as mentioned above, stage I does not occur in multiple slip conditions which prevail in the indentation problem). Note also that the calibrated value of $\tau_0 = 8\,\mathrm{MPa}$ is consistent with the range of values of the initial flow stress (from 4.5 MPa to 11.5 MPa) reported in Haasen (1958).

The material parameters used in the computations are summarized in Table 4. The elastic constants c_{ij} have been taken from literature (Hirth and Lothe, 1992). The hardening parameters $(\tau_0, \tau_{max}, \theta_0, \theta_{IV})$ have been calibrated as described above. The typical value of $q = 1.4$ has been adopted for the latent hardening

coefficient. The strengthening parameter a, cf. the Taylor formula (18), has been assumed equal to $a = 0.33$, which is an intermediate value from the range $a \approx 0.30$–0.36 typical for fcc metals (Sauzay and Kubin, 2011). Finally, the shear modulus on the $\{1\,1\,1\}\langle 1\,\bar{1}\,0\rangle$ slip system is $\mu = (c_{11} - c_{12} + c_{44})/3$, and the Burgers vector modulus of nickel is $b = 0.248\,\text{nm}$.

Table 4: Material parameters used in the simulations.

c_{11} [GPa]	c_{12} [GPa]	c_{44} [GPa]	τ_0 [MPa]	τ_{max} [MPa]	θ_0 [MPa]	θ_{IV} [MPa]	q	a	μ [GPa]	b [nm]
246.5	147.3	124.7	8	150	240	7.5	1.4	0.33	74.6	0.248

4.2 Results of finite-element computations

In this section, we report on the results of finite-element simulations of wedge indentation and compare the model predictions to the experimental results of Dahlberg et al. (2014) and Sarac et al. (2016). In those experiments, a nickel single crystal was indented into its $(0\,0\,1)$ plane by a sharp tungsten-carbide wedge. Three wedge indenters with the included angle of 60°, 90° and 120° were used in the experiment. The crystal was oriented such that the wedge was parallel to the $[1\,1\,0]$ direction so that plane-strain conditions prevailed within the $(1\,1\,0)$ plane, see Section 2.4. After indentation, the specimen midsection was exposed and local in-plane rotations near the indent were measured using the electron backscatter diffraction (EBSD) technique. The out-of-plane rotations were one order of magnitude smaller than the in-plane rotations, thus validating the plane-strain assumption.

The maximum indentation depth in the experiment was equal to 200 µm. However, this value includes a significant amount of elastic deflection in the experimental setup. This can be observed in Fig. 3 in Dahlberg et al. (2014), where the slope of the unloading branch of the load–penetration depth curves is fairly gentle, which is attributed to the elastic springback in the setup. Accordingly, the experimental load–penetration depth curves have been corrected here by subtracting the elastic deflection, assumed proportional to the load, from the measured penetration depth. The corresponding proportionality factor, i.e. the elastic compliance of the setup, has been adjusted such that the slope of the unloading branch approximately matches that predicted by the finite-element model for the 120° wedge. As a result of the correction procedure described above, the maximum indentation depth is reduced to 185–190 µm. The raw and the corrected experimental load–penetration depth curves are shown in Fig. 6 below. To comply with the corrected data, the finite-element simulations are here carried out for the maximum indentation depth $h_{max} = 185\,\mu\text{m}$.

In the finite-element model, the sharp wedge is approximated by a rounded one with the tip radius $r = 18.5\,\mu\text{m}$, ten times smaller than the indentation depth h_{max}, thus $r/h_{max} = 0.1$. The radius of the wedge tip used in the experiment was at least two orders of magnitude smaller, but the ratio $r/h_{max} = 0.1$ is the minimum one for which we could obtain the solution for the three wedge angles considered. For a smaller wedge angle, and also for a sharp wedge, the strains and mesh distortion at the tip are excessively large which causes severe convergence problems. Note that a significantly larger tip radius ($r/h_{max} = 0.5$) was used in the simulations of Dahlberg et al. (2014). The friction coefficient $f = 0.5$ has been assumed at the contact interface, which proved to yield reasonable results (a study of the effect of friction is reported in Appendix A).

The rate-dependent regularization of the Schmid law, cf. Section 2.1.1, has been used in the simulations reported in this subsection with the exponent $m = 40$ and the reference slip rate $\dot{\gamma}_0 = 10^{-3}\,1/\text{s}$. The maximum penetration depth $h_{max} = 185\,\mu\text{m}$ has been achieved in $t_{max} = 100\,\text{s}$ at the constant velocity $v = h_{max}/t_{max}$,

which has been adjusted such that the maximum indentation force does not differ significantly from that obtained using the rate-independent model, see Appendix B.

The mesh size in the vicinity of the indent has been chosen individually for each wedge angle in such a way that a similar number of nodes is in contact with the wedge at the maximum indentation depth. The mesh has been significantly coarsened far from the indent, as shown in Fig. 3 for the case of the 90° wedge. In order to reduce the computational cost, the symmetry of the problem has been exploited with the adequate symmetry conditions enforced on the displacements and non-local slip increments. The computational domain is a square with the side length equal to 5 mm, 5.2 mm and 8.8 mm for the wedge angles 60°, 90° and 120°, respectively. The domain size is sufficiently large so that the boundary conditions applied at the bottom and right edges of the domain do not influence the results. In fact, the plastic deformation is localized in the vicinity of the wedge, as shown in Fig. 4 for the 90° wedge. The deformed mesh in the vicinity of the indent after unloading is shown in Fig. 5 for all wedge angles. Large plastic deformation can be observed, especially for the 60° wedge.

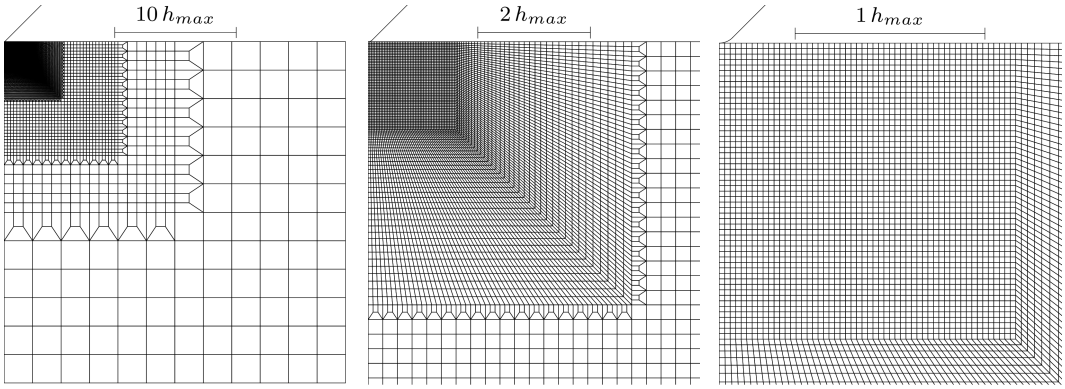

Figure 3: Finite-element mesh used in the simulations for the 90° wedge.

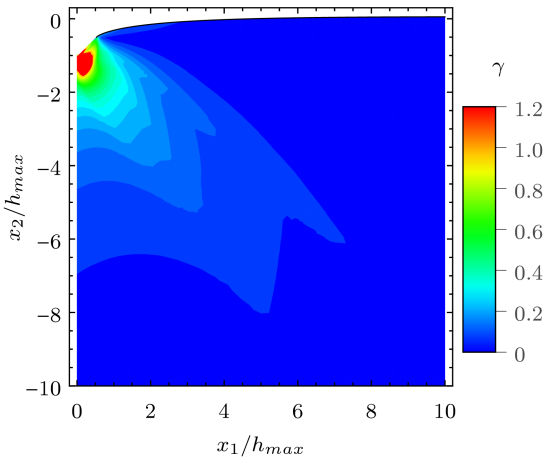

Figure 4: Accumulated effective slip γ after unloading (90° wedge).

The predicted load–penetration depth curves are compared to the experimental ones in Fig. 6 (the correction procedure that has been applied to the experimental curves is described above). It is recalled that the hardening curve (specifically, the initial flow stress τ_0) has been calibrated using only the experimental load–depth curve for the 120° wedge, cf. Fig 6c. The load–depth curves for the 60° and 90° wedges are here predicted using the same set of material parameters, and a good agreement with the experiment is apparent.

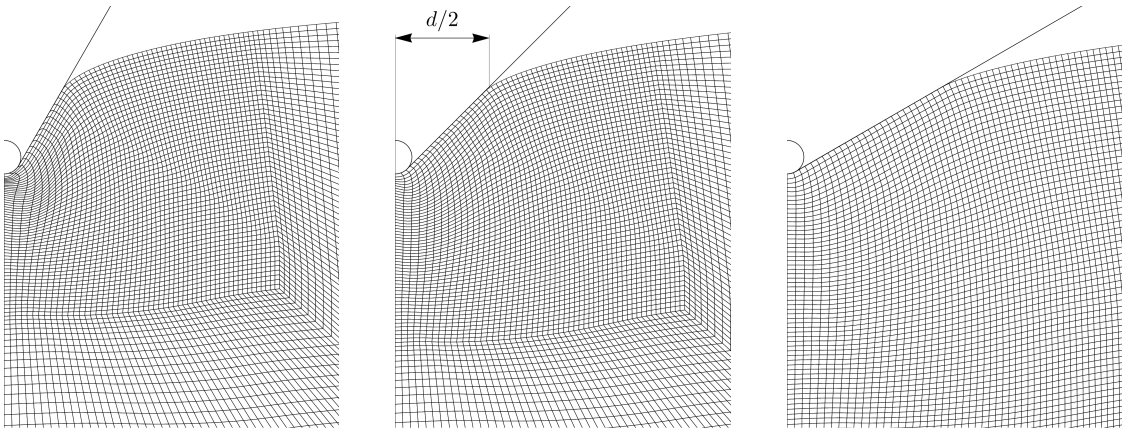

(a) 60° wedge (b) 90° wedge (c) 120° wedge

Figure 5: Deformed mesh in the vicinity of the indent.

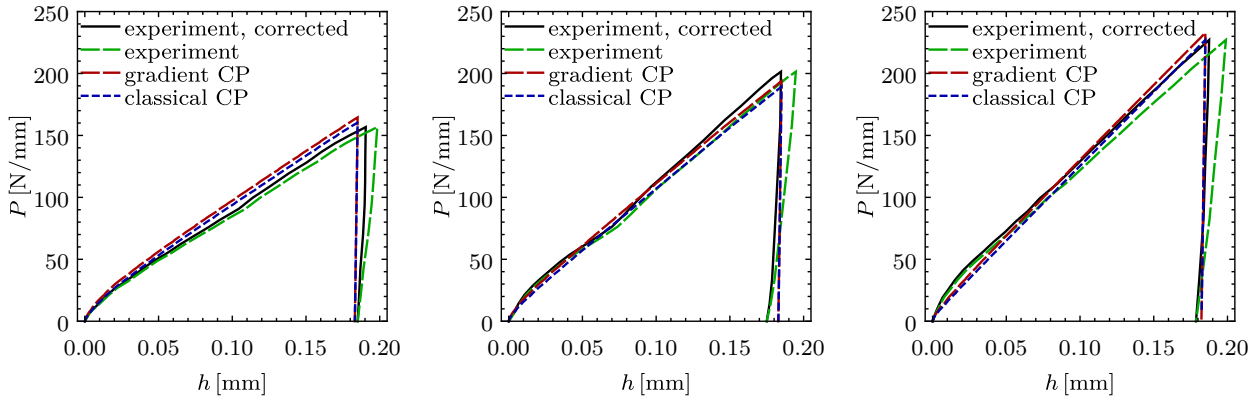

(a) 60° wedge (b) 90° wedge (c) 120° wedge

Figure 6: Load–penetration depth curves: finite-element predictions obtained using the classical and gradient crystal plasticity (CP) are compared to the corrected experimental data of Dahlberg et al. (2014). Also shown is the raw experimental curve which features an excessive elastic springback in the unloading branch.

Figure 6 includes the results obtained with and without the gradient enhancement in the hardening law, but the difference is small (about 2.5%). The maximum indentation depth is here relatively large ($h_{max} = 185\,\mu m$), and thus the gradient effects predicted by the model are not significant. This prediction seems physically correct, as visible size effects are expected for significantly smaller indentation depths. Note that, in wedge indentation into an aluminum single crystal, a visible increase of hardness has been obtained for the indentation depths below $10\,\mu m$ (Chen et al., 2012). Also, for the Berkovich or spherical tip, the indentation size effect has been observed (e.g., McElhaney et al., 1998; Swadener et al., 2002) for various materials at indentation depths smaller by at least one order of magnitude than the indentation depth of $185\,\mu m$ studied here.

A more detailed study of size effects is reported in Section 5 where the indentation response is simulated for a range of decreasing indentation depths. In that study, the wedge tip radius and the finite-element mesh are scaled accordingly to preserve geometrical similarity so that the size effect is solely due to the gradient effects. In Fig. 6, the differences between the curves for the classical and gradient crystal plasticity emerge at low indentation depths. However, the related size effects are influenced by the varying indenter geometry (because the wedge tip is rounded) and by the finite-element discretization (because the resolution is not sufficiently fine at the early stage of indentation).

In Fig. 7, the lattice rotations predicted by the present finite-element model are compared to the experimental lattice rotations obtained using EBSD (Dahlberg et al., 2014). Lattice rotation is here calculated by postprocessing the finite-element results, and it is equal to $\omega_3 = \arcsin(R^*_{21})$, where $\mathbf{R}^* = \mathbf{F}^*(\mathbf{U}^e)^{-1}$, cf. Eq. (1). It is apparent that the predicted lattice-rotation patterns are very similar to those observed experimentally. For each wedge angle, the predicted and measured lattice rotations are also compared along a horizontal line of constant x_2, see the diagrams in the right-hand column in Fig. 7. There is some ambiguity concerning the depth from which the experimental data was actually taken so that, for the model predictions, the depth has been adjusted to obtain a possibly good agreement with the experimental data. This depth is indicated by a horizontal line on each lattice rotation map in the middle column in Fig. 7. Again, the agreement can be considered very good. Note that the experimental results exhibit some fine features that are related to the inhomogeneity of plastic deformation at a lower scale, and these features are not reproduced by the crystal-plasticity model. As in the case of the load-depth curves, the effect of the gradient enhancement on the lattice rotation is not much pronounced, see the right-hand column in Fig. 7.

Sarac et al. (2016) have further processed the experimentally measured lattice rotations by evaluating their spatial derivatives in order to estimate the components of the dislocation density (Nye's) tensor $\boldsymbol{\alpha}$ evaluated in the deformed configuration, see also Kysar et al. (2007) and Dahlberg et al. (2014). The Nye's tensor $\boldsymbol{\alpha}$ delivers the net Burgers vector density $\mathbf{B} = \boldsymbol{\alpha}\mathbf{n}$ which is equal to the net (resultant) Burgers vector of the GNDs piercing the unit area of the plane of the unit normal $\mathbf{n}$. Under the assumption of plane-strain deformation[2] and neglecting the contribution of elastic strains, the Nye's tensor $\boldsymbol{\alpha}$ has only two non-zero components $\alpha_{13} \approx -\partial\omega_3/\partial x_1$ and $\alpha_{23} \approx -\partial\omega_3/\partial x_2$ (cf. Kysar et al., 2007; Sarac et al., 2016). Accordingly, for $\mathbf{n} = \mathbf{e}_3$, the net Burgers vector density $\mathbf{B} = (\alpha_{13}, \alpha_{23}, 0)$ fully quantifies the incompatibility of plastic deformation and the GND density. Figure 8a shows the magnitude $|\mathbf{B}|$ of the net Burgers vector density $\mathbf{B}$ determined by Sarac et al. (2016) according to the procedure described above for the 90° wedge. Note that in the plane-strain conditions we have $|\mathbf{B}| = ||\boldsymbol{\alpha}||$.

[2]The plane-strain assumption includes here the condition that the out-of-plane plastic strain rate L^p_{33} vanishes. This condition is automatically satisfied once the kinematics of the reduced 2D model is adopted, cf. Section 2.4.

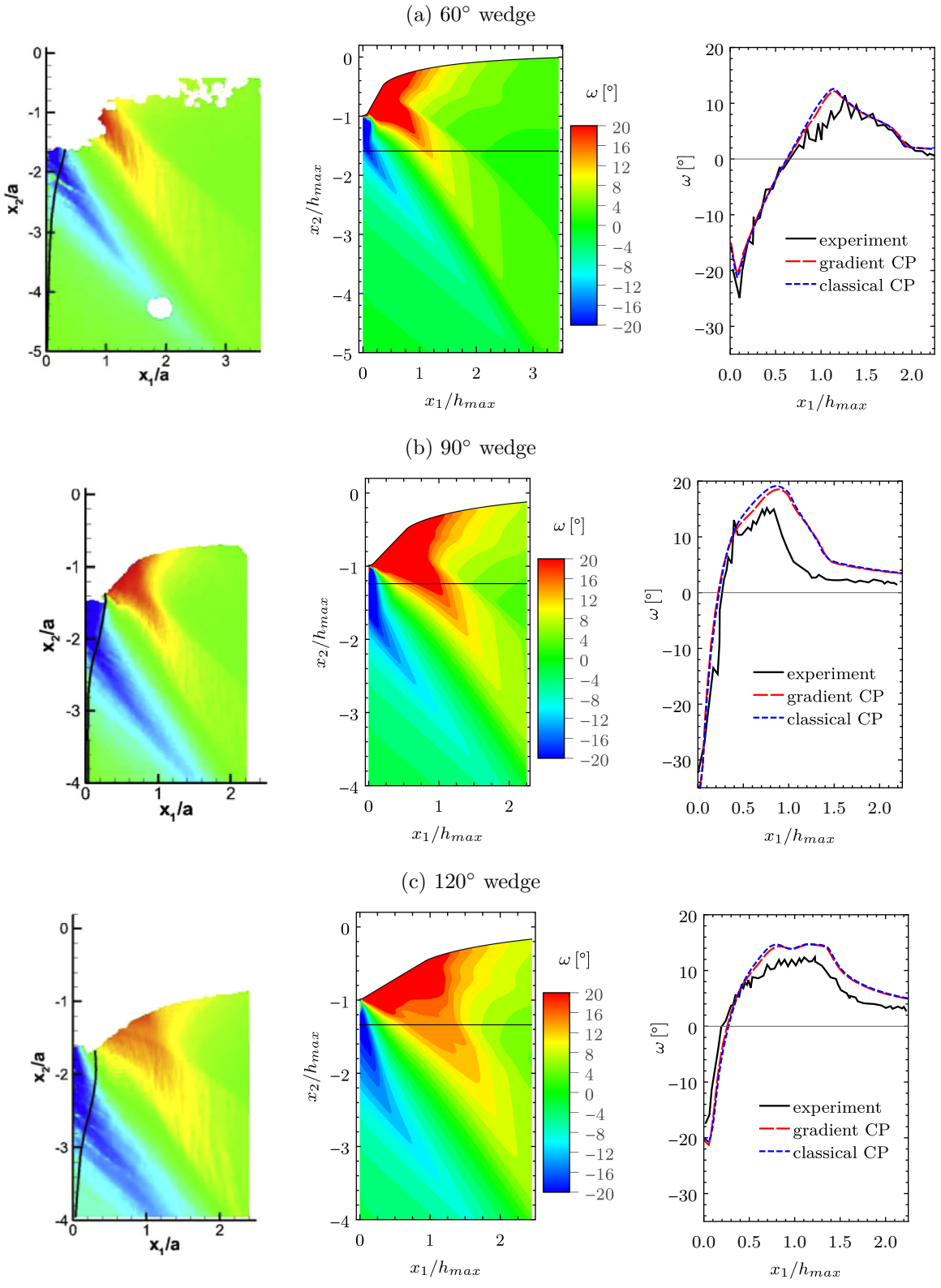

Figure 7: Lattice rotation maps obtained from the finite-element simulations (center, obtained using the classical CP model) compared to the experimental results of Dahlberg et al. (2014) (left, reproduced with permission from Elsevier). The plots in the right-hand column show the lattice rotation along the horizontal line indicated in the middle column (see text). The spatial coordinates are normalized by the maximum penetration depth h_{max} (which is denoted by a in Dahlberg et al. (2014)).

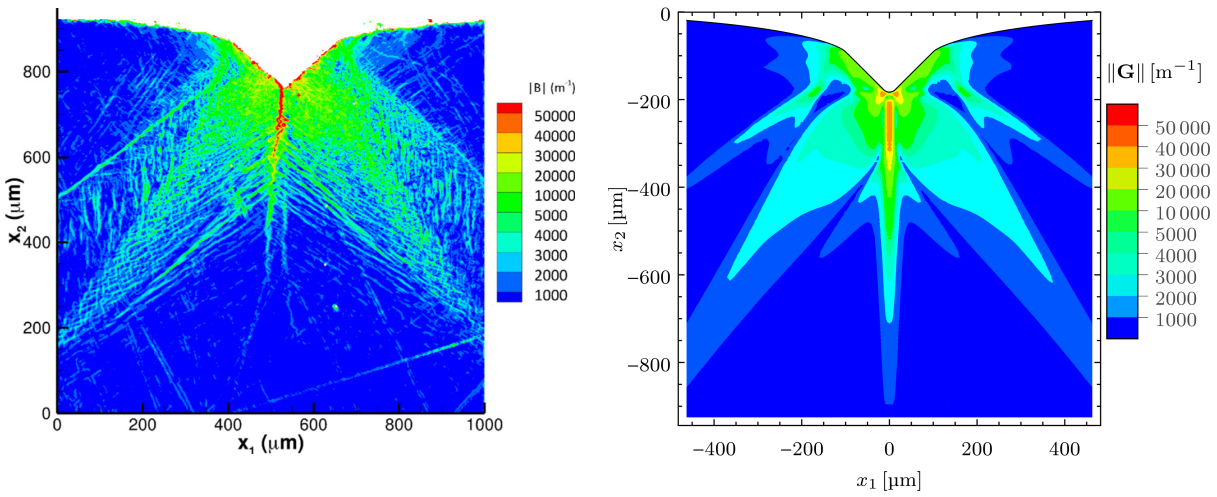

(a) experiment

(b) finite-element simulation

Figure 8: Distribution of GNDs near the indent for the 90° wedge: (a) the magnitude $|\mathbf{B}|$ of the net Burgers vector density $\mathbf{B}$ (Sarac et al., 2016, reproduced with permission from Elsevier); (b) the norm $||\mathbf{G}||$ of the dislocation density tensor $\mathbf{G}$ predicted by the gradient-enhanced model.

In the finite-deformation framework, the dislocation density tensor $\mathbf{G}$ is the counterpart of the Nye's tensor $\boldsymbol{\alpha}$ (cf. Cermelli and Gurtin, 2001). The norm of $\mathbf{G}$ predicted for the 90° wedge is shown in Fig. 8b for comparison with the experimental results in Fig. 8a. The agreement is satisfactory in terms of both the pattern and the magnitude, the latter treated in the average sense, since the experimental results exhibit fine features due to inhomogeneity of plastic deformation, as already discussed above. Both in the experiment and in the simulation, the GND density is the highest along the symmetry line, where the lattice rotation suffers a jump, or rather an abrupt change. However, in the simulation, the maximum values are lower than in the experiment, which is, at least partially, due to the limited spatial resolution of the finite-element mesh.

The dislocation density tensor $\mathbf{G}$ has been here obtained by integrating $\overset{\diamond}{\mathbf{G}}$, the plastically convected rate of $\mathbf{G}$, cf. Eq. (21). Note that $\overset{\diamond}{\mathbf{G}}$ is readily available in the computational model, as it is used to compute the effective slip-rate gradient $\dot{\chi}$, cf. Eq. (20).

The experimentally determined net Burgers vector density $\mathbf{B}$ has been further characterized by evaluating its orientation angle $\beta = \arctan(\alpha'_{23}/\alpha'_{13})$ that is defined in terms of the components of the Nye's tensor in the local coordinate system aligned with the lattice, see Sarac et al. (2016) for details. The field of β has been next filtered in order to eliminate small variations of β and also to reveal the boundaries of the slip-activity regions. The filtered field of β obtained for the 90° wedge is shown in Fig. 9a. In the finite-strain framework, the orientation angle β is defined in terms of the two non-zero components of the dislocation density tensor $\mathbf{G}$, namely $\beta = \arctan(G_{23}/G_{13})$. The corresponding map of β is shown in Fig. 9b and exhibits a reasonably good agreement with the experiment.

A quantitative comparison of the experimental and the predicted orientation angle β is presented in Fig. 10. Here, angle β is shown along four 90-degree circular arcs of radius R with the centre located at the intersection of the undeformed surface with the symmetry axis. The arcs are parameterized by angle θ with $\theta = -90°$ corresponding to the symmetry axis. For $R = 1.5\,h_{max}$ and $R = 2\,h_{max}$, i.e. close to the wedge tip, the predicted orientation angle β does not agree well with the experiment, in particular, next to the symmetry

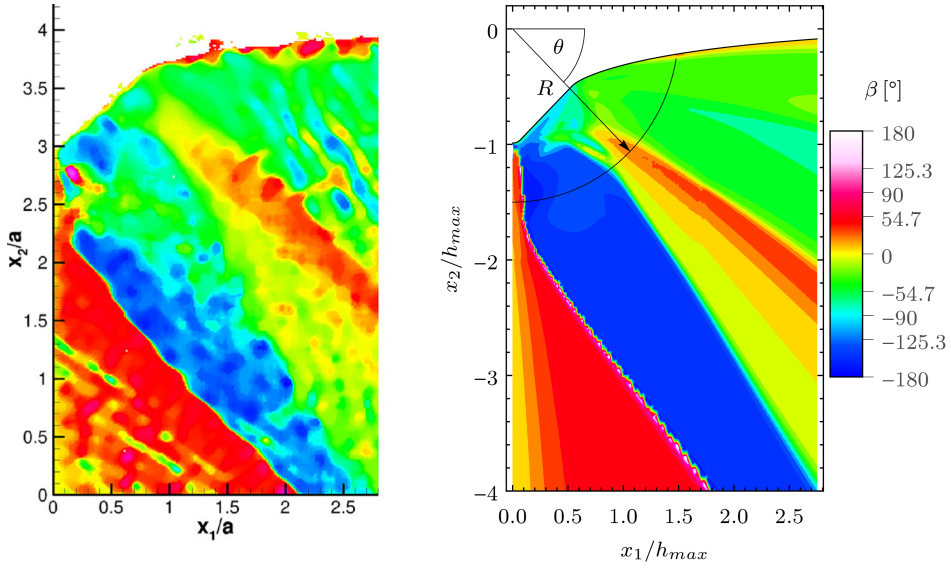

(a) experiment (b) finite-element simulation

Figure 9: Orientation of the net Burgers vector density **B** characterized by angle β: (a) experimental results of Sarac et al. (2016) (reproduced with permission from Elsevier); (b) finite-element predictions (for the 90° wedge).

axis. The difference may be due to rounding of the wedge tip that has been introduced in the finite-element model. At a greater distance from the wedge tip, for $R = 2.5\,h_{max}$ and $R = 3\,h_{max}$, the simulation results are consistent with the experiment. It can also be seen in Fig. 10 that the results obtained using the model with and without the gradient enhancement in the hardening law are very similar. This confirms that, as already concluded earlier, the size effects are not significant for the relatively large indentation depth of 185 µm.

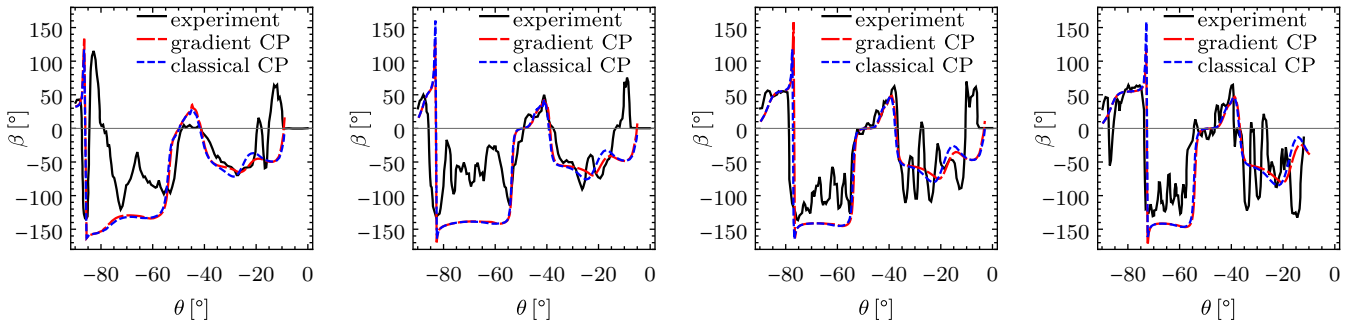

(a) $R = 1.5\,h_{max}$ (b) $R = 2\,h_{max}$ (c) $R = 2.5\,h_{max}$ (d) $R = 3\,h_{max}$

Figure 10: Angle β along the circular arcs of radius R for the 90° wedge: experimental results (Sarac et al., 2016) and model predictions.

Summarizing, the simulations reported in this subsection show a good qualitative and quantitative agreement with the experiment both in terms of the load–penetration depth response and in terms of the lattice rotation and incompatibility. Such a consistent set of simulations of the wedge indentation problem, covering the three wedge angles used in the experiment, has not been reported so far, even if selected features could be represented reasonably well in the earlier modelling of wedge indentation (Dahlberg et al., 2014; Reuber et al., 2014; Sarac et al., 2016). We believe that the good performance of the present computational model is due to

the consistent reduction of the general 3D crystal plasticity model to the 2D plane-strain model (Section 2.4) combined with the careful calibration of the hardening law (Section 4.1). Furthermore, thanks to the robust finite-element implementation, the computations have been performed using a relatively fine finite-element mesh and a relatively small tip radius.

Finally, we note that the detailed experimental characterization of the lattice rotation and the subsequent processing of these data (Dahlberg et al., 2014; Sarac et al., 2016) reveal fine features related to the inhomogeneity of plastic deformation, see the experimental results in Figs. 7–9. Similar features can be observed in other experimental studies of wedge indentation (Kysar et al., 2007, 2010; Gan, 2008). These effects are not captured by the present model nor by other continuum models used in the simulations of wedge indentation (Dahlberg et al., 2014; Reuber et al., 2014; Baitsch et al., 2015; Sarac et al., 2016).

5 Size effects

The indentation depth $h_{max} = 185\,\mu\text{m}$, as employed in the wedge indentation experiments of Dahlberg et al. (2014), is relatively large, and the indentation response is expected to be unaffected by the size effects. This has been confirmed by the simulations reported in Section 4.2. Thus, in this section, we study the size effects, as predicted by the gradient-enhanced crystal-plasticity model, by examining the wedge indentation also for smaller indentation depths. Comparison to experimental data is not performed here because no relevant data is available. The only published experimental results on the size effect in wedge indentation are those obtained by Chen et al. (2012) for aluminum. However, characterization of material properties is missing so that calibration of the model is not possible.

A series of simulations of the wedge indentation problem has been performed for the indentation depth h_{max} ranging from 200 µm down to 1 µm. To preserve geometrical similarity, the ratio of the wedge tip radius to the maximum indentation depth is kept constant, $r/h_{max} = 0.1$. The finite-element mesh is also scaled with h_{max} such that the element size h is proportional to h_{max}. The length-scale parameter l_h in the averaging equation (32) is assumed equal to the finite-element size h, thus $l_h = h$, cf. Section 3. The influence of this parameter on the size effects predicted by the model is illustrated in Appendix C.

Figure 11 shows the normalized load–penetration depth curves that correspond to the maximum indentation depth h_{max} varied between 200 µm and 1 µm. The curves are normalized by dividing both the penetration depth h and the indentation load P by the maximum penetration depth h_{max}. Accordingly, the size effect manifests itself in the dependence of the normalized load–penetration depth curve on the maximum penetration depth. Indeed, it can be seen that, for all wedge angles, the maximum normalized load increases significantly (approximately by the factor of 2.5) when the maximum penetration depth h_{max} decreases from 200 µm to 1 µm.

The size effect is even more pronounced in terms of the hardness, cf. Fig. 12. The hardness H is here defined as the maximum load P_{max} divided by the corresponding projected contact area d, thus $H = P_{max}/d$, where d is the width of the contact zone projected onto the initial surface, see Fig. 5. Figure 12a shows the hardness H as a function of the maximum penetration depth h_{max}, while Fig. 12b shows the relative increase of hardness with respect to the large penetration-depth limit H_0. For $h_{max} = 1\,\mu\text{m}$, the relative increase in hardness exceeds 4.2 for the 60° wedge and 3.6 for the 120° wedge. In general, the hardness is higher for a sharper wedge in the whole range of penetration depths, in agreement with experimental observations (Chen et al., 2012). In Fig. 12c, the normalized hardness H/H_0 is shown as a function of the contact width d.

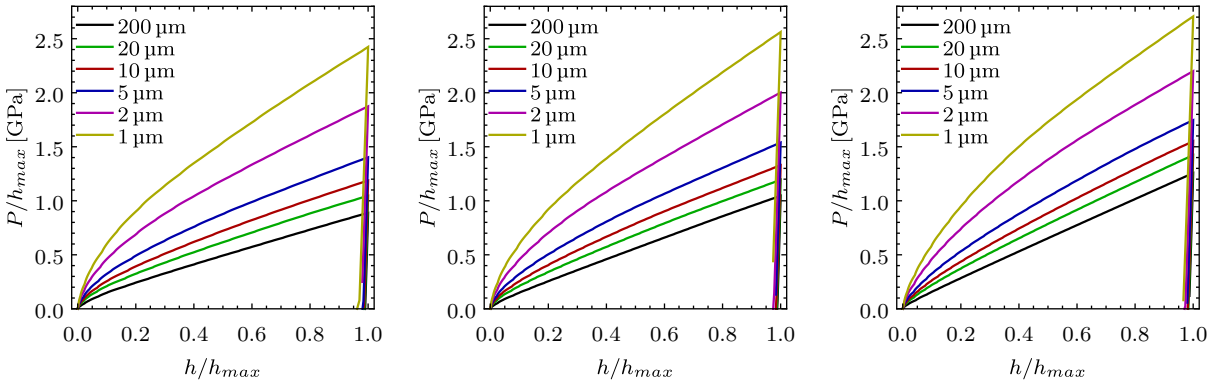

(a) 60° wedge (b) 90° wedge (c) 120° wedge

Figure 11: Dependence of the normalized load–penetration depth curve on the maximum penetration depth h_{max}. The individual curves correspond to h_{max} varied between 200 µm and 1 µm.

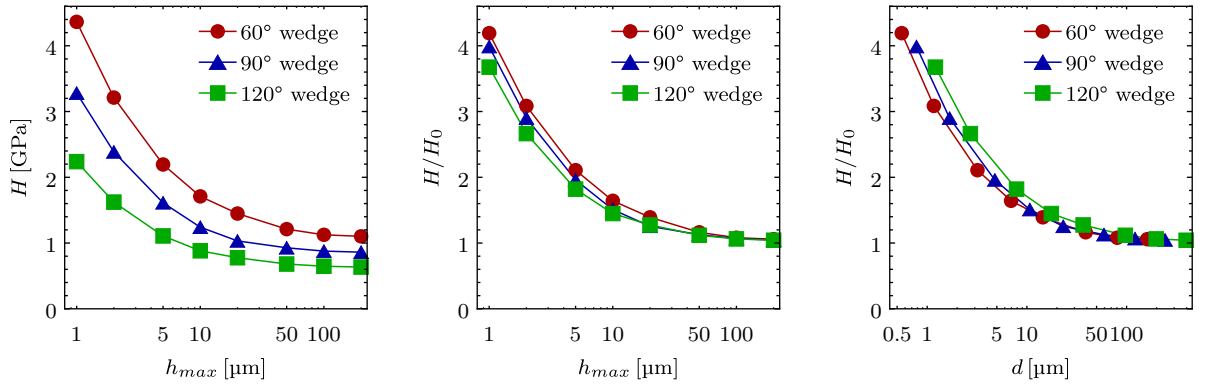

(a) (b) (c)

Figure 12: The predicted size effect on the indentation hardness in wedge indentation: (a) hardness H as a function of the maximum penetration depth h_{max}; (b) normalized hardness H/H_0 as a function of h_{max}; (c) H/H_0 as a function of the contact width d.

The model developed by Nix and Gao (1998) by considering a conical indenter and an idealized distribution of GNDs predicts that the squared hardness is a linear function of the inverse of the maximum indentation depth such that $(H/H_0)^2 = 1 + h^*/h_{max}$ where h^* is a characteristic length. The corresponding representation of the indentation size effect predicted by the present model is shown in Fig. 13. It can be seen that the dependence of the squared hardness on the inverse of h_{max} is indeed approximately linear in the range of indentation depths studied here. Note, however, that the range of indentation depths that has been examined does not include very small depths for which a breakdown in linearity is often observed in experiment (e.g., Pharr et al., 2010).

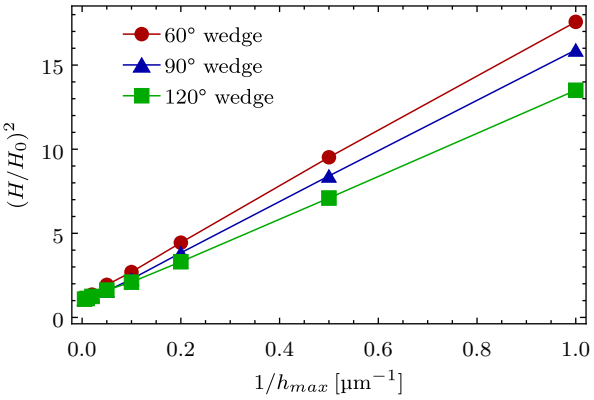

Figure 13: Dependence of the squared hardness $(H/H_0)^2$ on the inverse of the maximum indentation depth h_{max}. The dependence is approximately linear in agreement with the model of Nix and Gao (1998).

Figure 14 shows the size effect on the residual imprint. It can be seen that the sink-in is more pronounced for smaller h_{max}, and this is associated with the decrease of the normalized contact width d/h_{max} as h_{max} decreases. The latter effect is responsible for the increase in hardness by the factor of approximately four in the considered range of h_{max}, as compared to the corresponding increase in the maximum normalized load by the factor of approximately 2.5, cf. Fig. 6. Qualitatively, the sink-in behaviour predicted here for the wedge indentation is similar to that predicted by Stupkiewicz and Petryk (2016) for spherical indentation into a (100)-oriented Cu single crystal. The residual imprint consists then of four pile-up and four sink-in regions, and the size effect manifests itself in less piling-up and more sinking-in as the indenter radius decreases (while keeping a fixed ratio of the maximum indentation depth to the indenter radius).

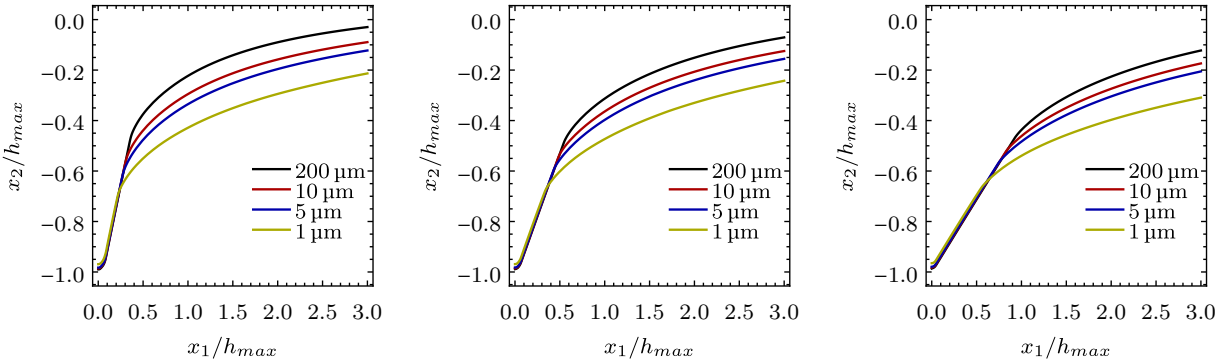

(a) 60° wedge (b) 90° wedge (c) 120° wedge

Figure 14: Effect of the maximum indentation depth h_{max} (varied between 200 μm and 1 μm) on the profile of the residual imprint.

The influence of the additional hardening due to slip-rate gradients on the plastic flow is also illustrated in Fig. 15 which shows the lattice rotation maps for the 90° wedge for five selected maximum indentation depths. The general pattern of lattice rotation is not size-dependent and, in all cases, exhibits two elongated zones of negative and positive rotation. However, a visible reduction of the rotation angle can be observed as h_{max} is decreased. The same effect is also observed for the 60° and 120° wedges.

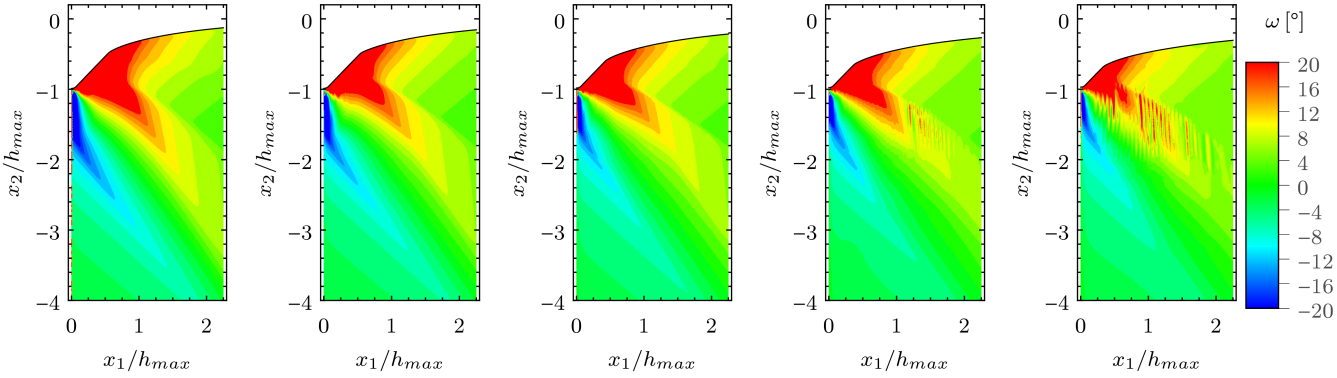

(a) $h_{max} = 200\,\mu m$ (b) $h_{max} = 20\,\mu m$ (c) $h_{max} = 5\,\mu m$ (d) $h_{max} = 2\,\mu m$ (e) $h_{max} = 1\,\mu m$

Figure 15: Effect of the maximum indentation depth h_{max} on the lattice rotation map (for the 90° wedge).

Figure 15 illustrates yet another effect, namely, spurious oscillations of lattice rotation within the elongated zone of positive rotation. The oscillations appear for the smallest penetration depth $h_{max} = 1\,\mu m$; they are also visible, but less pronounced for $h_{max} = 2\,\mu m$. The oscillations correlate with mesh spacing which indicates that the response is mesh-dependent as a result of a kind of instability (this may suggest that the regularization delivered by the averaging equation (32) with $l_h = h$ is here insufficient). While inhomogeneity, e.g., deformation banding, is a typical feature of plastic deformation, the particular appearance of the deformation patterns obtained should be treated as a numerical artefact. The corresponding results are thus less reliable even if, overall, they seem consistent with the remaining results.

The size effect is particularly pronounced in Fig. 16 which shows the magnitude of the net Burgers vector density represented by the norm $\|\mathbf{G}\|$ of the dislocation density tensor $\mathbf{G}$. Since $\mathbf{G}$ is computed in terms of the slip-rate gradients, the value of $\mathbf{G}$ is, to the first order, inversely proportional to the maximum penetration depth h_{max}, and hence it increases with decreasing h_{max}. Clearly, this scaling is at the very origin of the GND hardening and of the related indentation size effect because the magnitude of the net Burgers vector density is a measure of the density of GNDs. At the same time, the GND hardening influences plastic flow below the indenter, as already discussed above. This results in a size-dependent pattern of the distribution of $\|\mathbf{G}\|$ shown in Fig. 16. Note that the values corresponding to the respective contours (and colours) in Fig. 16 are scaled proportionally to the inverse of h_{max} so that the significant differences in the appearance of the individual contour plots in Fig. 16 result from the differences in the plastic flow. The spurious oscillations of lattice rotation that occur for $h_{max} = 2\,\mu m$, Fig. 15d, result also in oscillations of $\|\mathbf{G}\|$ that are visible in Fig. 16c, even if less pronounced than in the case of lattice rotation.

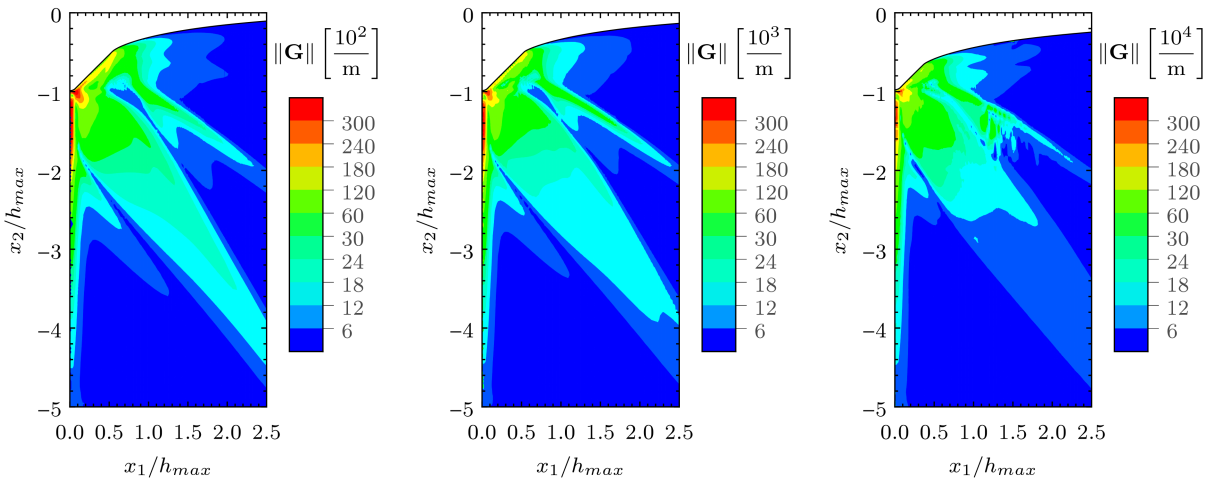

(a) $h_{max} = 200\,\mu\mathrm{m}$ (b) $h_{max} = 20\,\mu\mathrm{m}$ (c) $h_{max} = 2\,\mu\mathrm{m}$

Figure 16: Effect of the maximum indentation depth h_{max} on the magnitude of the net Burgers vector density represented by $\|\mathbf{G}\|$ (for the 90° wedge). Note that the scaling of the contour values is inversely proportional to $h_{\max}$.

6 Conclusion

A comprehensive study of wedge indentation into a nickel single crystal has been performed using the gradient-enhanced crystal-plasticity model proposed recently by Petryk and Stupkiewicz (2016). The model has been first applied to simulate the wedge indentation experiments reported by Dahlberg et al. (2014) and Sarac et al. (2016). For the indentation depth of about 200 µm, as employed in the experiment, the response is practically not affected by the size effects. In terms of the maximum load, the difference between the gradient-enhanced model and the classical non-gradient model is about 2.5%. We have demonstrated that all major features of the experimental response obtained for three wedge angles can be very well reproduced using a single set of material parameters.

The non-gradient Voce-like hardening law has been calibrated using the data available in the literature. Only one parameter, the initial critical resolved shear stress, has been adjusted such that the maximum load predicted for the 120° wedge matches the experiment. Importantly, the adopted values of the hardening parameters fall well within the corresponding ranges established in the materials science literature. A physically relevant calibration of the non-gradient hardening law is important because the gradient enhancement of the hardening law, as proposed by Petryk and Stupkiewicz (2016), is in a sense automatic. The internal length scale is expressed solely in terms of the standard parameters of the non-gradient hardening law, and there is no adjustable parameter in the gradient-enhanced hardening law.

After the model has been validated against the experiment, the indentation size effect has been examined by simulating wedge indentation for a range of indentation depths decreasing from 200 µm down to 1 µm. In this range of indentation depths, the size effect manifests itself in the increase of hardness by the factor of approximately four with respect to the large penetration-depth limit. This is also accompanied by size-dependence of other features, including the residual imprint. In particular, the sink-in is more pronounced for smaller indentation depths. In the whole range of penetration depths, the hardness exhibits a strong dependence on the wedge angle, the hardness corresponding to the 60° wedge being about twice higher than

that corresponding to the 120° wedge. At the same time, the normalized hardness, when expressed as a function of the indentation depth or contact width, shows only a weak dependence on the wedge angle. Qualitatively, this observation is consistent with the experimental results reported by Chen et al. (2012) for an aluminum single crystal. As illustrated in Appendix C, the primary size effect governed by the gradient-enhanced hardening law is influenced by a secondary effect due to the averaging operation which is introduced in the computational model and which involves an independent length-scale parameter.

As an intermediate, apparently new result, the general 3D crystal-plasticity model has been consistently reduced to a 2D plane-strain model that involves three effective in-plane slip systems. The original idea of such reduction is due to Rice (1987) who, however, considered an ideally plastic crystal only. For a hardening crystal, the structure of the hardening law is preserved in the reduced model. However, the effective slip-system interaction matrix takes a non-trivial form, and the effective slip rate is not a simple sum, but rather a weighted sum of the slip rates on the individual effective in-plane slip systems.

Acknowledgement This work has been supported by the National Science Center (NCN) in Poland through Grant No. 2014/13/B/ST8/04286. The authors gratefully acknowledge stimulating discussions with Prof. Henryk Petryk.

A Effect of friction at the contact interface

The effect of friction at the contact interface has been studied by simulating the wedge indentation problem for four values of the friction coefficient $f = 0.1$, 0.3, 0.5 and 0.7. The 90° wedge has been selected as the representative reference case. The gradient-enhanced hardening law has been used in this study to check whether the friction stresses at the contact interface and the related shear deformation in the subsurface layer induce additional hardening. As in Section 4.2, the rate-dependent regularization of the Schmid law has been used.

The load–penetration depth curves are presented in Fig. 17a, and, quite surprisingly, the influence of the friction coefficient on this global response is practically negligible. However, the local deformation pattern below the wedge tip does depend on the friction coefficient. For instance, for $f = 0.1$, the mesh below the wedge tip is highly distorted, cf. Fig. 18a, which is because the small friction forces do not prevent sliding along the wedge surface. With increasing friction coefficient, the distortion becomes significantly smaller, cf. Fig. 18b, and it stabilizes for $f = 0.5$, cf. Fig. 18c. This may indicate that, for $f = 0.5$ or higher, the friction is high enough to prevent sliding, and sticking friction prevails.

Despite the visible differences in the local deformation pattern below the wedge tip, the lattice rotation fields are not much affected by the friction coefficient, see Fig. 19. A careful examination reveals that the lattice rotation map corresponding to the lowest friction coefficient $f = 0.1$ differs slightly from the remaining maps. This difference is better visible in Fig. 17b where the lattice rotation is shown at a fixed depth (in the deformed configuration).

To conclude, the results are not much affected when the friction coefficient f is varied between 0.3 and 0.7. For $f = 0.1$, some differences can be observed, but such a low friction coefficient does not seem realistic. Based on the results of the present parametric study, the friction coefficient $f = 0.5$ has been used in the remaining computations reported in this paper.

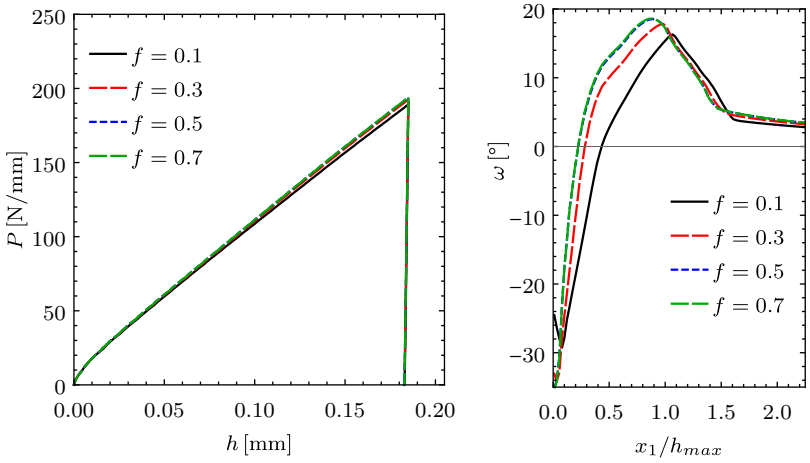

(a) (b)

Figure 17: Influence of the friction coefficient f on: (a) load–penetration depth response for the 90° wedge; (b) lattice rotation along the horizontal line at a fixed depth below the wedge tip, cf. Fig. 7b.

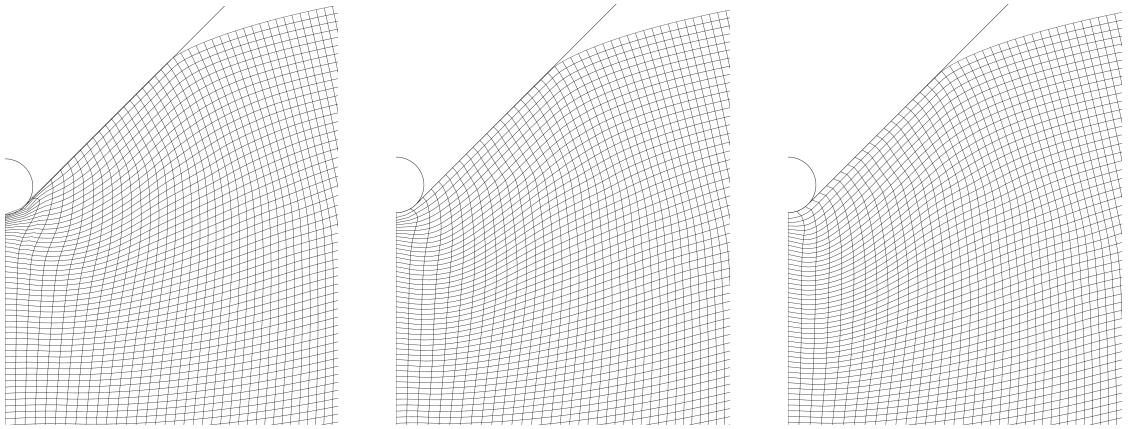

(a) $f = 0.1$ (b) $f = 0.3$ (c) $f = 0.5$

Figure 18: Deformed finite-element mesh in the vicinity of the wedge tip for (a) $f = 0.1$, (b) $f = 0.3$ and (c) $f = 0.5$.

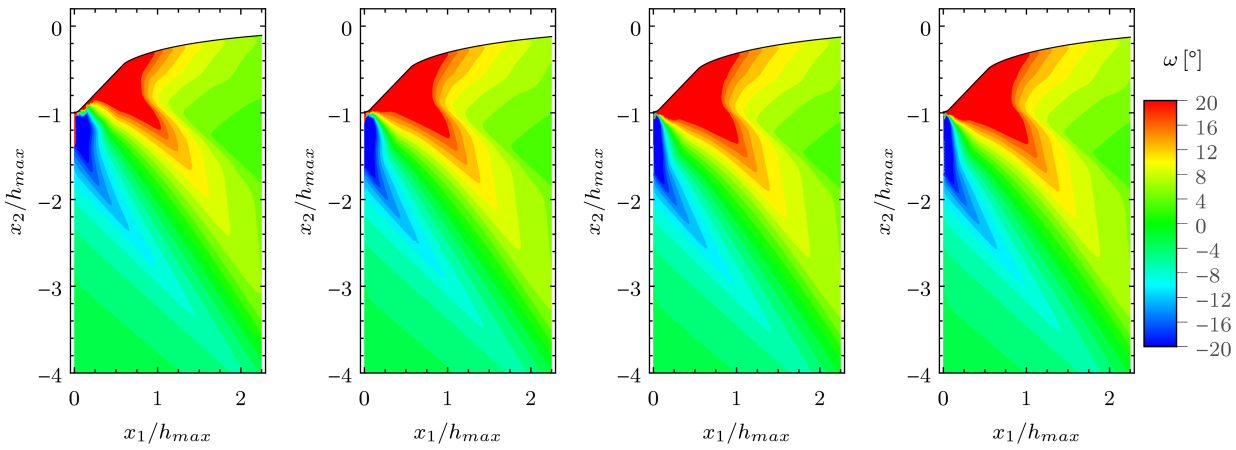

(a) $f = 0.1$ (b) $f = 0.3$ (c) $f = 0.5$ (d) $f = 0.7$

Figure 19: Influence of the friction coefficient f on the lattice rotation.

B Influence of the regularization scheme

It is of interest to investigate whether and how the regularization scheme applied to the Schmid law influences the predictions delivered by the crystal-plasticity model, and selected results of the corresponding parametric study are reported in this appendix. The wedge indentation problem has thus been simulated by employing the two regularization schemes described in Section 2.1 with three values of the rate-sensitivity exponent $m = 20, 40, 100$ in the case of the rate-dependent regularization, cf. Eq. (7), and with three values of the regularization exponent $n = 6, 10, 20$ in the case of the rate-independent regularization, cf. Eq. (8). We recall that the rate-sensitivity exponent $m = 40$ has been used in the simulations reported in Sections 4 and 5, while the exponent $n = 20$ has been used in the 3D simulations reported in Stupkiewicz and Petryk (2016). Since the classical crystal-plasticity model and the gradient-enhanced model yield very similar results for $h_{max} = 185\,\mu\text{m}$, only the latter model is considered here.

The results of the simulations prove that the impact of the regularization scheme on the response is negligible for the considered range of the regularization parameters m and n. This is illustrated in Fig. 20, which shows the load–penetration depth curves, and in Fig. 21, which shows the lattice rotation along a horizontal line at a fixed depth below the wedge tip. Those results show also that the rate-sensitivity exponent $m = 40$, used in the remainder of this paper, is sufficiently high so that the results are not visibly affected by this parameter.

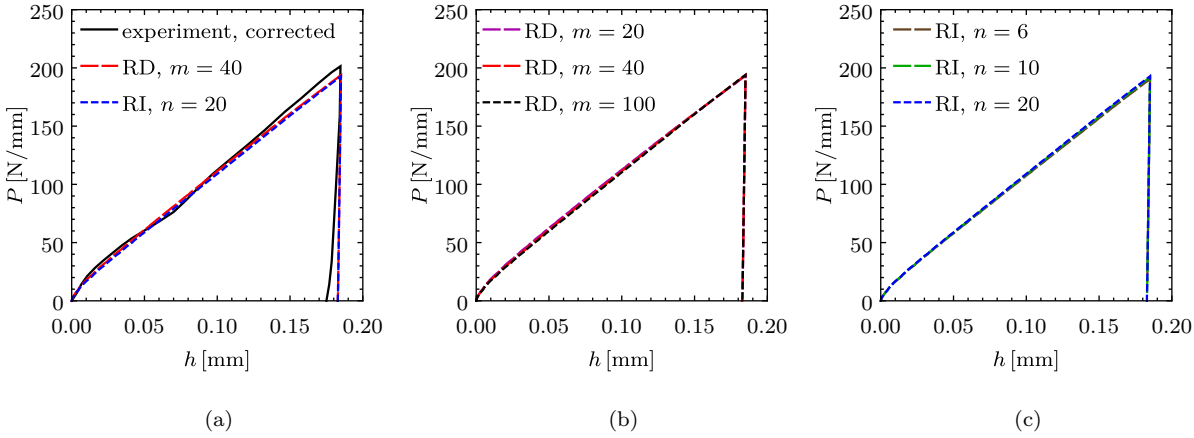

Figure 20: Load–penetration depth curves for the 90° wedge: (a) results obtained for the rate-dependent (RD) and rate-independent (RI) regularization are compared to the experimental curve; (b) the effect of the rate-sensitivity exponent m of the RD regularization scheme; (c) the effect of the exponent n of the RI regularization scheme.

According to our experience, in the case of the reduced 2D plane-strain crystal-plasticity model with the gradient-enhanced hardening law, the rate-independent regularization performs significantly worse than the rate-dependent regularization, especially when the specimen size is reduced (as in the study in Section 5). The rate-dependent regularization has thus been used in the simulations reported in Sections 4 and 5. Note, however, that the rate-independent regularization has been successfully employed in 3D simulations of spherical indentation using the classical crystal-plasticity (Petryk et al., 2017) and the gradient-enhanced crystal-plasticity model (Stupkiewicz and Petryk, 2016).

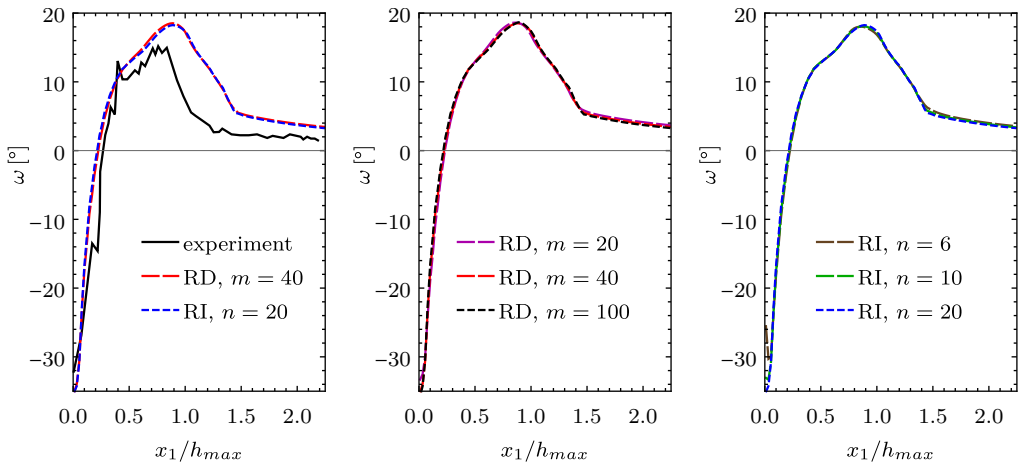

(a) (b) (c)

Figure 21: Lattice rotation ω for the 90° wedge, cf. Fig. 7: (a) results obtained for the rate-dependent (RD) and rate-independent (RI) regularization are compared to the experimental curve; (b) the effect of the rate-sensitivity exponent m of the RD regularization scheme; (c) the effect of the exponent n of the RI regularization scheme.

C Influence of the length-scale parameter l_h

In this appendix, we illustrate how the indentation size effect predicted by the present gradient-enhanced crystal-plasticity model is influenced by the length-scale parameter l_h that governs the averaging delivered by Eq. (32). The study is here limited to the case of the 120° wedge, in which the deformations are smaller, and the mesh distortion is less pronounced than in the case of the 60° and 90° wedges, and thus the computational model is then more robust.

In addition to $l_h = h$, as employed in Section 5, the simulations have thus been carried out for $l_h = 2h$. It is recalled that the element size h is kept proportional to the maximum indentation depth h_{max}, cf. Section 5, and hence l_h, treated as a numerical parameter, is proportional to h_{max}. The resulting dependence of the normalized hardness H/H_0 on the maximum indentation depth h_{max} and on the contact width d is shown in Fig. 22. It can be seen that the increase of l_h results in a reduction of the hardness. This effect can be explained by observing that the increase of l_h leads to excessive averaging of the local slip rates $\dot{\gamma}_\alpha$ so that the gradients of the non-local slip-rates $\dot{\bar{\gamma}}_\alpha$ are reduced, and so is the additional hardening due to GNDs.

As discussed in Section 3, instead of prescribing the ratio of l_h/h, a constant value of parameter l_h can be prescribed so that l_h can be interpreted as an additional material parameter. The results corresponding to $l_h = 50\,\text{nm}$ and $l_h = 100\,\text{nm}$ are depicted in Fig. 22. As in the case of l_h proportional to h, discussed above, the increase of l_h results in a reduction of the hardness.

The selected value of $l_h = 50\,\text{nm}$ is close to the element size $h = 37\,\text{nm}$ in the case of the smallest maximum indentation depth of $h_{max} = 1\,\mu\text{m}$. Accordingly, for $h_{max} = 1\,\mu\text{m}$, the hardness predicted for $l_h = 50\,\text{nm}$ is close to that for $l_h = h$ (likewise, the hardness predicted for $l_h = 100\,\text{nm}$ is close to that for $l_h = 2h$). For large penetration depths, e.g., for $h_{max} = 200\,\mu\text{m}$, the indentation size effect is negligible, and thus $H/H_0 \approx 1$ regardless of the value of l_h. In the intermediate range of h_{max}, the value of l_h visibly influences the dependence of the hardness on h_{max}.

Concluding, the length-scale parameter l_h has been shown to visibly influence the predicted indentation size

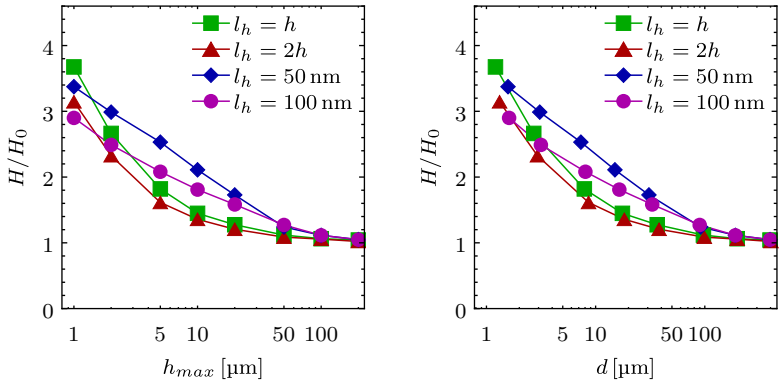

(a) (b)

Figure 22: Influence of the length-scale parameter l_h on the indentation size effect predicted for the 120° wedge: the normalized hardness H/H_0 as a function of the maximum penetration depth h_{max} (a) and of the contact width d (b).

effect. The natural length scale ℓ is responsible for the primary effect due to slip-rate gradients, as described by the gradient-enhanced hardening law (19). In the present computational treatment, the secondary effect of the parameter l_h cannot be fully separated from this primary effect because of the opposite effects of excessive smoothing, when l_h is increased, and insufficient regularization, when l_h is decreased. In particular, the latter effect may manifest itself in spurious oscillations, such as those visible in Fig. 15e. It is thus an open problem how to adjust the numerical length-scale parameter l_h in the averaging equation (32), or how to formulate the model without resorting to such averaging.

References

R. K. Abu Al-Rub. Prediction of micro and nanoindentation size effect from conical or pyramidal indentation. *Mech. Mater.*, 39(8):787–802, 2007.

P. Alart and A. Curnier. A mixed formulation for frictional contact problems prone to Newton like solution methods. *Comput. Methods Appl. Mech. Eng.*, 92(3):353–375, 1991.

L. Anand, M. E. Gurtin, and B. D. Reddy. The stored energy of cold work, thermal annealing, and other thermodynamic issues in single crystal plasticity at small length scales. *Int. J. Plast.*, 64:1–25, 2015.

M. Arminjon. A regular form of the schmid law. Application to the ambiguity problem. *Texture Microstruct.*, 14(18):1121–1128, 1991.

R. J. Asaro. Crystal plasticity. *J. Appl. Mech.*, 50:921–934, 1983.

M. F. Ashby. The deformation of plastically non-homogeneous materials. *Philos. Mag.*, 21(170):399–424, 1970.

M. Baitsch, K. C. Le, and T. M. Tran. Dislocation structure during microindentation. *Int. J. Eng. Sci.*, 94: 195–211, 2015.

D. S. Balint, V. S. Deshpande, A. Needleman, and E. Van der Giessen. Discrete dislocation plasticity analysis of the wedge indentation of films. *J. Mech. Phys. Solids*, 54(11):2281–2303, 2006.

S. Bargmann, B. Svendsen, and M. Ekh. An extended crystal plasticity model for latent hardening in polycrystals. *Comput. Mech.*, 48(6):631–645, 2011.

J. L. Bassani and T. Y. Wu. Latent hardening in single crystals. II. Analytical characterization and predictions. *Proc. R. Soc. London, Ser. A*, 435:21–41, 1991.

E. Bittencourt. On the effects of hardening models and lattice rotations in strain gradient crystal plasticity simulations. *Int. J. Plast.*, 2018. doi: 0.1016/j.ijplas.2018.05.004.

P. Cermelli and M. E. Gurtin. On the characterization of geometrically necessary dislocations in finite plasticity. *J. Mech. Phys. Solids*, 49(7):1539–1568, 2001.

K. Chen, W. J. Meng, and G. B. Sinclair. Size dependence of the plane-strain response of single-crystal Al to indentation by diamond wedges. *Acta Mater.*, 60(12):4879–4887, 2012.

C. F. O. Dahlberg, Y. Saito, M. S. Öztop, and J. W. Kysar. Geometrically necessary dislocation density measurements associated with different angles of indentations. *Int. J. Plast.*, 54:81–95, 2014.

E. Demir, D. Raabe, N. Zaafarani, and S. Zaefferer. Investigation of the indentation size effect through the measurement of the geometrically necessary dislocations beneath small indents of different depths using EBSD tomography. *Acta Mater.*, 57(2):559–569, 2009.

L. P. Evers, W. A. M. Brekelmans, and M. G. D. Geers. Scale dependent crystal plasticity framework with dislocation density and grain boundary effects. *Int. J. Solids Struct.*, 41(18):5209–5230, 2004.

N. A. Fleck and J. W. Hutchinson. A phenomenological theory for strain gradient effects in plasticity. *J. Mech. Phys. Solids*, 41(12):1825–1857, 1993.

N. A. Fleck, G. M. Muller, M. F. Ashby, and J. W. Hutchinson. Strain gradient plasticity: Theory and experiment. *Acta Metall. Mater.*, 42(2):475–487, 1994.

S. Forest, R. Sievert, and E. C. Aifantis. Strain gradient crystal plasticity: Thermomechanical formulations and applications. *J. Mech. Behav. Mater.*, 13(3-4):219–232, 2002.

P. Franciosi and A. Zaoui. Multislip in f.c.c. crystals a theoretical approach compared with experimental data. *Acta Metall.*, 30(8):1627–1637, 1982.

W. Gambin. Refined analysis of elastic-plastic crystals. *Int. J. Solids Struct.*, 29(16):2013–2021, 1992.

Y. X. Gan. Analysis of stress and deformation states in wedge indented face-centered cubic single crystals. *Mater. Sci. Eng. A*, 485(1):589–600, 2008.

Y.F. Gao, B.C. Larson, J.H. Lee, L. Nicola, J.Z. Tischler, and G.M. Pharr. Lattice rotation patterns and strain gradient effects in face-centered-cubic single crystals under spherical indentation. *J. Appl. Mech.*, 82 (6):061007, 2015.

J.R. Greer and W.D. Nix. Nanoscale gold pillars strengthened through dislocation starvation. *Phys. Rev. B*, 73:245410, 2006.

M. E. Gurtin. On the plasticity of single crystals: free energy, microforces, plastic-strain gradients. *J. Mech. Phys. Solids*, 48(5):989–1036, 2000.

M. E. Gurtin. A finite-deformation, gradient theory of single-crystal plasticity with free energy dependent on densities of geometrically necessary dislocations. *Int. J. Plast.*, 24:702–725, 2008.

P. Haasen. Plastic deformation of nickel single crystals at low temperatures. *Philos. Mag.*, 3(28):384–418, 1958.

C. S. Han, H. Gao, Y. Huang, and W. D. Nix. Mechanism-based strain gradient crystal plasticity - I. Theory. *J. Mech. Phys. Solids*, 53(5):1188–1203, 2005.

R. Hill. Generalized constitutive relations for incremental deformation of metal crystals by multislip. *J. Mech. Phys. Solids*, 14(2):95–102, 1966.

R. Hill and J. R. Rice. Constitutive analysis of elastic-plastic crystals at arbitrary strain. *J. Mech. Phys. Solids*, 20(6):401–413, 1972.

J. P. Hirth and J. Lothe. *Theory of Dislocation*. Krieger Publishing Company, Malabar, Florida, 1992.

T. Hochrainer, S. Sandfeld, M. Zaiser, and P. Gumbsch. Continuum dislocation dynamics: Towards a physical theory of crystal plasticity. *J. Mech. Phys. Solids*, 63:167–178, 2014.

L. Hollang. *Purification Process and Characterization of Ultra High Purity Metals: Application of Basic Science to Metallurgical Processing*, chapter Mechanical Properties. Springer Science & Business Media, 2002.

Y. Huang, H. Gao, W. D. Nix, and J. W. Hutchinson. Mechanism-based strain gradient plasticity—II. Analysis. *J. Mech. Phys. Solids*, 48(1):99–128, 2000.

Y. Huang, S. Qu, K. C. Hwang, M. Li, and H. Gao. A conventional theory of mechanism-based strain gradient plasticity. *Int. J. Plast.*, 20(4):753–782, 2004.

Y. Huang, F. Zhang, K. C. Hwang, W. D. Nix, G. M. Pharr, and G. Feng. A model of size effects in nano-indentation. *J. Mech. Phys. Solids*, 54(8):1668–1686, 2006.

J. W. Hutchinson. Bounds and self-consistent estimates for creep of polycrystalline materials. *Proc. R. Soc. London A*, 348:101–127, 1976.

U. F. Kocks. Constitutive behavior based on crystal plasticity. In Alan K. Miller, editor, *Unified Constitutive Equations for Creep and Plasticity*, pages 1–88. Springer Netherlands, 1987.

U. F. Kocks and H. Mecking. Physics and phenomenology of strain hardening: the FCC case. *Prog. Mater Sci.*, 48(3):171–273, 2003.

J. Korelc. Multi-language and multi-environment generation of nonlinear finite element codes. *Eng. Comput.*, 18(4):312–327, 2002.

J. Korelc and P. Wriggers. *Automation of Finite Element Methods*. Springer, 2016.

J. Korelc, U. Ŝolinc, and P. Wriggers. An improved EAS brick element for finite deformation. *Comput. Mech.*, 46(4):641–659, 2010.

J. Kratochvil and M. Kruzik. Statistically motivated model of mechanisms controlling evolution of deformation band substructure. *Int. J. Plast.*, 81:196–208, 2016.

H. G. M. Kreuzer and R. Pippan. Discrete dislocation simulation of nanoindentation: Indentation size effect and the influence of slip band orientation. *Acta Mater.*, 55(9):3229–3235, 2007.

E. Kröner. Allgemeine Kontinuumstheorie der Versetzungen und Eigenspannungen. *Arch. Ration. Mech. Anal.*, 4:273–334, 1960.

E. Kröner. Dislocations and continuum mechanics. *Appl. Mech. Rev.*, 15:599–606, 1962.

M. Kuroda and V. Tvergaard. A finite deformation theory of higher-order gradient crystal plasticity. *J. Mech. Phys. Solids*, 56(8):2573–2584, 2008.

J. W. Kysar, Y. X. Gan, T. L. Morse, X. Chen, and M. E. Jones. High strain gradient plasticity associated with wedge indentation into face-centered cubic single crystals: geometrically necessary dislocation densities. *J. Mech. Phys. Solids*, 55(7):1554–1573, 2007.

J. W. Kysar, Y. Saito, M. S. Oztop, D. Lee, and W. T. Huh. Experimental lower bounds on geometrically necessary dislocation density. *Int. J. Plast.*, 26(8):1097–1123, 2010.

E. H. Lee. Elastic-plastic deformation at finite strains. *J. Appl. Mech.*, 36(1):1–6, 1969.

W. B. Lee and Y. P. Chen. Simulation of micro-indentation hardness of FCC single crystals by mechanism-based strain gradient crystal plasticity. *Int. J. Plast.*, 26(10):1527–1540, 2010.

Q. Ma and D. R. Clarke. Size dependent hardness of silver single crystals. *J. Mater. Res.*, 10(4):853–863, 1995.

J. Mandel. Plasticité classique et viscoplasticité. *CISM Lectures Notes*, 97, 1971.

K. W. McElhaney, J. J. Vlassak, and W. D. Nix. Determination of indenter tip geometry and indentation contact area for depth-sensing indentation experiments. *J. Mater. Res.*, 13(5):1300–1306, 1998.

W. D. Nix and H. Gao. Indentation size effects in crystalline materials: a law for strain gradient plasticity. *J. Mech. Phys. Solids*, 46(3):411–425, 1998.

J. F. Nye. Some geometrical relations in dislocated crystals. *Acta Metall.*, 1(2):153–162, 1953.

M. Ortiz and L. Stainier. The variational formulation of viscoplastic constitutive updates. *Comput. Methods Appl. Mech. Eng.*, 171(3):419–444, 1999.

R. Peerlings, R. De Borst, and J. H. P. De Vree. Gradient enhanced damage for quasi-brittle materials. *Int. J. Numer. Methods Eng.*, 39:3391–3403, 1996.

H. Petryk and M. Kursa. Incremental work minimization algorithm for rate-independent plasticity of single crystals. *Int. J. Numer. Methods Eng.*, 104(3):157–184, 2015.

H. Petryk and S. Stupkiewicz. A minimal gradient-enhancement of the classical continuum theory of crystal plasticity. Part I: The hardening law. *Arch. Mech.*, 68(6):459–485, 2016.

H. Petryk, S. Stupkiewicz, and S. Kucharski. On direct estimation of hardening exponent in crystal plasticity from the spherical indentation test. *Int. J. Solids Struct.*, 112:209–221, 2017.

G. M. Pharr, E. G. Herbert, and Y. Gao. The indentation size effect: A critical examination of experimental observations and mechanistic interpretations. *Annu. Rev. Mater. Res.*, 40(1):271–292, 2010.

A. Popp, B. I. Wohlmuth, M. W. Gee, and W. A. Wall. Dual quadratic mortar finite element methods for 3D finite deformation contact. *SIAM J. Sci. Comput.*, 34(4):421–446, 2012.

S. Qu, Y. Huang, G. M. Pharr, and K. C. Hwang. The indentation size effect in the spherical indentation of iridium: A study via the conventional theory of mechanism-based strain gradient plasticity. *Int. J. Plast.*, 22 (7):1265–1286, 2006.

M. Rester, C. Motz, and R. Pippan. Indentation across size scales – A survey of indentation-induced plastic zones in copper 111 single crystals. *Scr. Mater.*, 59(7):742–745, 2008.

C. Reuber, P. Eisenlohr, F. Roters, and D. Raabe. Dislocation density distribution around an indent in single-crystalline nickel: Comparing nonlocal crystal plasticity finite-element predictions with experiments. *Acta Mater.*, 71:333–348, 2014.

J. R. Rice. Inelastic constitutive relations for solids: an internal-variable theory and its application to metal plasticity. *J. Mech. Phys. Solids*, 19(6):433–455, 1971.

J. R. Rice. Tensile crack tip fields in elastic-ideally plastic crystals. *Mech. Mater.*, 6(4):317–335, 1987.

P. A. Sabnis, S. Forest, N. K. Arakere, and V. A. Yastrebov. Crystal plasticity analysis of cylindrical indentation on a Ni-base single crystal superalloy. *Int. J. Plast.*, 51:200–217, 2013.

A. Sarac, M. S. Oztop, C. F. O. Dahlberg, and J. W. Kysar. Spatial distribution of the net Burgers vector density in a deformed single crystal. *Int. J. Plast.*, 85:110–129, 2016.

M. Sauzay and L. P. Kubin. Scaling laws for dislocation microstructures in monotonic and cyclic deformation of fcc metals. *Prog. Mater Sci.*, 56(6):725–784, 2011.

J. S. Stölken and A. G. Evans. A microbend test method for measuring the plasticity length scale. *Acta Mater.*, 46(14):5109–5115, 1998.

S. Stupkiewicz and H. Petryk. A minimal gradient-enhancement of the classical continuum theory of crystal plasticity. Part II: Size effects. *Arch. Mech.*, 68(6):487–513, 2016.

J. G. Swadener, E. P. George, and G. M. Pharr. The correlation of the indentation size effect measured with indenters of various shapes. *J. Mech. Phys. Solids*, 50(4):681–694, 2002.

G. I. Taylor. The mechanism of plastic deformation of crystals. Part I. Theoretical. *Proc. R. Soc. London, Ser. A*, 145(855):362–387, 1934.

A. J. Wilkinson and D. Randman. Determination of elastic strain fields and geometrically necessary dislocation distributions near nanoindents using electron back scatter diffraction. *Philos. Mag.*, 90(9):1159–1177, 2010.

S. Wulfinghoff, S. Forest, and T. Boehlke. Strain gradient plasticity modeling of the cyclic behavior of laminate microstructures. *J. Mech. Phys. Solids*, 79:1–20, 2015.

N. Zaafarani, D. Raabe, R. N. Singh, F. Roters, and S. Zaefferer. Three-dimensional investigation of the texture and microstructure below a nanoindent in a Cu single crystal using 3D EBSD and crystal plasticity finite element simulations. *Acta Mater.*, 54(7):1863–1876, 2006.

Y. Zhang, Y. Gao, and L. Nicola. Lattice rotation caused by wedge indentation of a single crystal: dislocation dynamics compared to crystal plasticity simulations. *J. Mech. Phys. Solids*, 68:267–279, 2014.